Title

Human spermatogenesis leads to a reduced nuclear pore structure and function

Authors

Ália dos Santos[1], Oliver Knowles[1], Tom Dendooven[1], Thomas Hale[1], Alister Burt[1,2], Piotr Kolata[1], Giuseppe Cannone[1], Dom Bellini[1], David Barford[1] and Matteo Allegretti[1*]

[1]Structural Studies Division, MRC Laboratory of Molecular Biology, Cambridge, UK
[2]Current address: Department of Structural Biology, Genentech Inc., South San Francisco, CA, USA
*Corresponding author

Abstract

Nuclear pore complexes (NPCs) are nuclear gateways which regulate transit of molecules larger than 40kDa through a Ran-dependent transport. The somatic human NPC scaffold consists of three stacked rings: cytoplasmic, nucleoplasmic, and inner ring, which define an approximately 55nm-wide central channel. However, how NPC architecture accommodates the different function of non-somatic cells is largely unknown.

Here, we reveal the *in-cell* architecture of the human sperm NPC exhibiting a central channel less than 40nm-wide, outlined exclusively by the inner ring. This is accompanied by a 6-fold reduction in nuclear diffusion and mis-localization of Ran-dependent transport components. We also unveil a septin filaments meshwork connecting the NPCs and postulate a mechanical role in channel constriction. Furthermore, we show the end of meiosis as the key differentiation step for NPC architectural changes.

Our work uses an integrative approach comprising electron-cryo-tomography, super-resolution-light-microscopy and biochemistry, to investigate macromolecular structure/ function in human physiological contexts.

Up to 10 Key words

Nuclear Pore Complex (NPC), electron cryo tomography (cryo-ET), cryo-Focussed Ion Beam milling (cryo-FIB), differentiation, light microscopy, sperm, nuclear transport, in-cell structural biology, cell biology

Introduction

In eukaryotic cells, the nucleus stores and protects the genetic information by enclosing it within a double lipid membrane, the nuclear envelope (NE). At the NE, large 110MDa protein complexes, known as nuclear pore complexes (NPCs), stabilise holes and allow regulated bidirectional transport and material exchange between the nucleus and the cytoplasm. NPCs are therefore crucial in the regulation of gene expression[1-4].

The structure of NPCs consists of three stacked multi-subunit rings surrounding a central channel of approximately 55nm diameter: two outer rings - the cytoplasmic and nuclear rings (CR and NR, respectively) - and the inner ring (IR), which sits at the point of fusion between the two lipid membranes. An additional ring, the luminal ring (LR), lies within the intermembrane space, around the IR[5-7] (Supp Fig. 1A). Each of these rings consists of multiple proteins, known as nucleoporins (NUPs), organised as supramolecular assemblies. In humans, scaffold NUPs form the IR and two Y-complex

rings that lie at the interface with both the CR and NR[8]. Additional proteins anchor to the Y-complex to form either the cytoplasmic filaments at the CR side of the NPC[9-13] at later stages of assembly[14,15], or to form the nuclear basket that extends from the NR into the nucleoplasm[16] (Supp Fig. 1A). The nuclear basket is critical for mRNA export[17,18] and nuclear import[19].

Several CR, NR and IR subunits contain phenylalanine-glycine (FG) repeats that extend towards the middle of the central channel[20]. Molecules below 40kDa in size can passively diffuse through the NPC, whilst transport of larger proteins is highly regulated[21-23]. This is achieved through interactions of FG repeats at the central channel with transport receptors and the small GTPase Ran[22]. Importantly, Ran determines transport directionality by creating a Ran gradient that is dependent on its nucleotide status – enrichment of Ran-GTP in the nucleus and Ran-GDP in the cytoplasm[24,25].

At the CR side of the NPC, RanBP2, also known as NUP358, stabilises two Y-complex-ring assemblies[26] and binds RanGAP, the Ran-activating protein, which ensures enrichment of Ran-GDP in the cytoplasm. RanBP2 is therefore critical in the regulation of nucleocytoplasmic trafficking[27]. Additionally, RanBP2 is a central component of NPCs present at stacked endoplasmic reticulum (ER) sheets, known as annulate lamellae[28-31]. These structures have been proposed to act as NPC storage pools during postmitotic NE assembly[32] and animal development[28,30,33,34].

NPCs are dynamic complexes capable of dilating and contracting to adapt to their mechanical environments[13,35-40]. This has been shown under several physiological conditions[35,40-42] and during differentiation[43,44]. NPCs extracted from cells[26,45], at annulatae lamellae[31], or in energy-depleted cells[40] display the highest reported levels of constriction, with a central channel diameter smaller than 50nm. NPC constriction has been also associated to slower passive diffusion of small molecules into the nucleus[38]. Among mechanical forces acting on the NE, membrane tension, modulated by cytoskeletal forces, for example, is considered to be a major contributor to changes in NPC dynamics[40,41,46]. Importantly, cytoskeletal forces are essential during nuclear reshaping in cell differentiation[47], tissue development and cell migration[48]. One prominent example of this phenomenon is spermiogenesis, the post-meiotic differentiation of male germ cells in testes. During this process, the nucleus of spermatids (post-meiotic cells) undergoes radical changes that culminate in the formation of mature spermatozoa which are capable of delivering the paternal DNA to the oocyte during fertilization[49-51]. These changes include DNA hyper-condensation through the replacement of histones with protamines, and elongation of the nucleus into a drop-shaped structure[50,51]. This is accompanied by time-sensitive regulation of protein expression, transcription shutdown and downregulation of nuclear transport[52-54]. Importantly, NPCs are also redistributed to the caudal region of the sperm head into redundant NE regions[55,56]. Previous work has suggested that several NUPs are critical during spermiogenesis[57-60]. However, it is unknown whether NPC architecture is altered in germ cells or if structural changes affect nuclear trafficking. This knowledge is particularly relevant to the study of early embryo development, as the whole paternal nucleus is delivered intact to the oocyte during fertilisation[61,62].

Here, we investigate the architecture and function of human sperm NPCs using an *in situ* integrative structural biology approach. We use a combination of electron-cryo-

tomography (cryo-ET), super-resolution light microscopy, immunohistochemistry in human tissue and biochemical approaches, to reveal a highly constricted and reduced NPC scaffold with altered nuclear transport in human sperm.

Results

Clustering of NPCs in human sperm cells.

In somatic cells, NPCs are distributed ubiquitously across the NE (Supp Fig. 1B). To investigate the localisation of NPCs in human sperm cells, we analysed samples from 25 healthy human donors. Using the MAb414 antibody as a marker for NPCs, we imaged human sperm cells with Structured Illumination Microscopy (SIM). Similarly to what was previously shown[55,56,63], we confirmed that NPCs are exclusively localised at the rear of the nucleus (Fig. 1A). 3D SIM reconstruction revealed that NPCs form a pocket surrounding the rear of the sperm head and flanking the tail (Fig. 1B; Supp Fig. 1C).

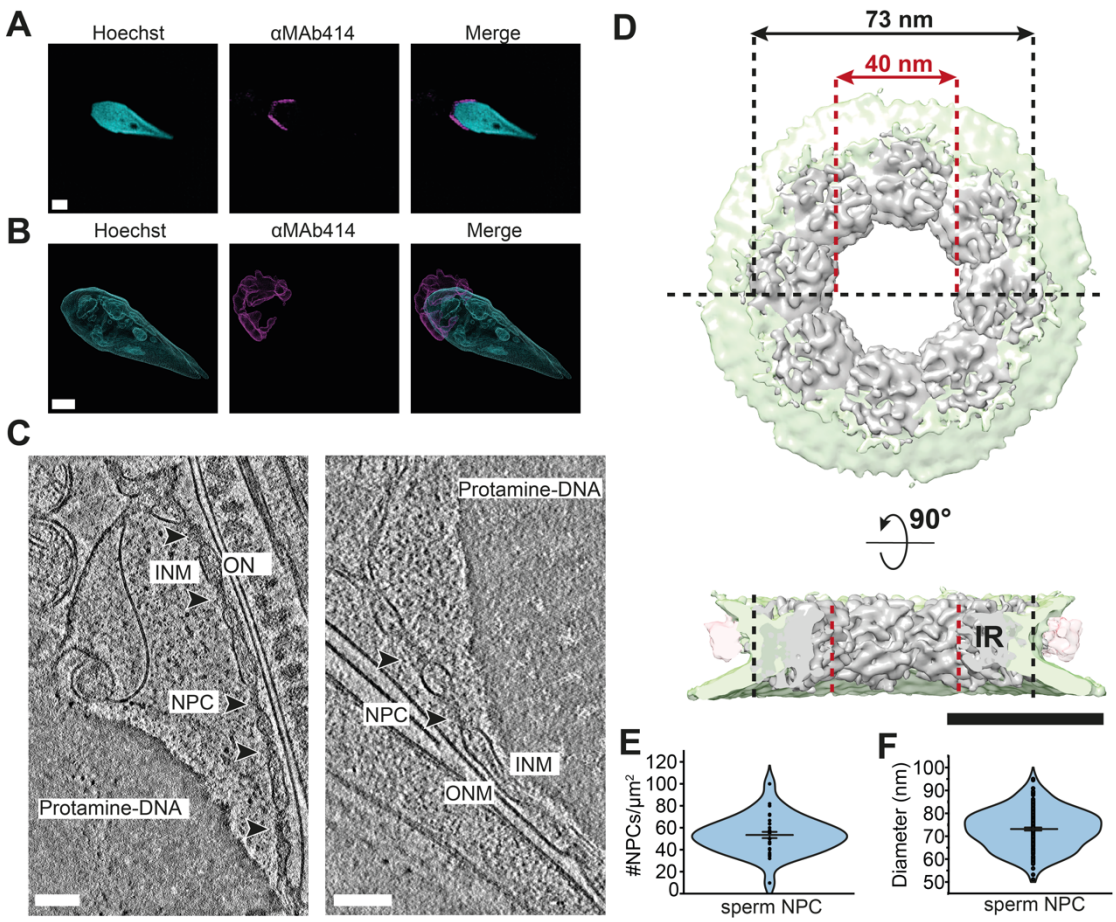

Figure 1 – *In-cell architecture* of the human sperm NPC. (A) Structured Illumination Microscopy (SIM) of NPCs in human sperm cells. DNA stained with Hoechst shown in cyan and NPCs at the rear of the nucleus immunolabelled with antibody MAb414, shown in magenta. Scale bar = 1µm. **(B)** 3D SIM reconstruction of the NPC region in the sperm cell shown in (**A**). Scale bar = 1µm. **(C)** 2D slices of reconstructed tomograms of the NPC regions of two human sperm cells. Condensed DNA (Protamine-DNA), Inner Nuclear Membrane (INM) and Outer Nuclear Membrane (ONM) are shown. NPCs are indicated with arrowheads. Scale bar = 100 nm. **(D)** *In-situ* structure of human sperm NPC – top view (above) and cross-sectional view (below). Inner Ring (IR) is shown in grey, nuclear membrane is shown in light green, luminal ring (LR) in light pink. Central channel diameter is indicated with red dashed lines and measured at 40nm; membrane-

to-membrane diameter (dashed black lines) is measured at 73nm. Scale bar = 50nm. **(E)** Violin plot with quantification of number of NPCs per nuclear membrane surface area in human sperm, from tomography data. Mean ± SE = 54 ± 3 NPCs/μm^2, n= 34 sperm cells. **(F)** Membrane-to-membrane diameter measurements of human sperm NPC from tomography data. Mean ± SE = 73.1 ± 0.7nm, n=174 NPCs.

A limitation of using fluorescence microscopy to understand the organisation of protein complexes, is the lack of cellular context. To visualise individual human sperm NPCs in their native environment at higher resolution, we used cryo-ET[35]. Following vitrification of human sperm cells on cryo-EM grids, we used cryo-focused ion beam (cryo-FIB) milling for sample thinning. This was followed by tilt-series acquisition on the produced lamellae at NPC regions at the rear of the sperm head. The reconstructed tomograms (Fig. 1C) show the Inner Nuclear Membrane (INM) and the Outer Nuclear Membrane (ONM) with several NPCs stacked along a stretch of NE (Fig. 1C, arrowheads). Using this volumetric data, we measured NPC density in the targeted regions as 54± 3 NPCs/μm^2 (Fig. 1E). This represents an approximately 7-fold increase in density relative to 5-10 NPCs/μm^2 present at the NE[64-66] of somatic cells, indicating a high degree of NPC clustering in human sperm cells.

***In-situ* architecture of the human sperm NPC reveals the absence of cytoplasmic and nuclear rings and a highly constricted central channel.**

Next, we investigated the structure of the human sperm NPC by performing subtomogram averaging[8], which resulted in a 3D density map of the native architecture of the complex (Fig. 1D; Supp Fig. 1D-G).

Unlike human somatic NPCs (Supp Fig. 1G)[13,26], our *in-situ* average of the human sperm NPC showed that only the IR was present, and no signal for the CR, NR and nuclear basket was present in the subtomogram average (Fig. 1D, Supp Fig. 1D, E and G, Supp movie 1). Furthermore, our cryo-ET data revealed a mean membrane-to-membrane NPC diameter of approximately 73nm and a central channel less than 40nm wide (Fig. 1D and F, Supp Fig. 1G). Compared to reported values of 92-105nm (membrane-to-membrane) and 54-60nm (central channel) for the *in-situ* NPCs in three different human cell lines[13,39,67] (Supp Fig. 1G); and 82-89nm (membrane-to-membrane) and 42-43nm (central channel) for the constricted *ex-cellulo* NPC[13,26], our data indicates that the human sperm NPC adopts a highly constricted conformation at the NE *in-cellulo*.

Notably, our *in-situ* structure did not show densities accounting for the presence of the Y-complex (Fig. 1D, Supp Fig. 1D, E and G, Supp movie 1). To validate this, we performed immunoblotting and immunofluorescent labelling and SIM against the Y-complex component NUP107[8,68] in sperm cells. Our data show that, in agreement with our structural model, NUP107 is absent in mature human sperm cells (Fig. 2A and E).

We also tested for the presence of RanBP2 and TPR to validate the absence of the CR and NR, respectively, using immunoblotting and immunofluorescence labelling. In agreement with our structural data, immunofluorescence detected only low levels of both proteins, notably not co-localised with NPCs (Fig. 2B and C; Supp Fig. 2F and G). Moreover, the presence of both components could not be detected through immunoblotting of human sperm lysates (Fig. 2F and G). Conversely, NUP93, a component of the IR, was detected and perfectly co-localised with MAb414 (Fig. 2D

and H). All these proteins were detected in human fibroblasts and co-localised at the NE with MAb414 (Supp Fig. 2A-E).

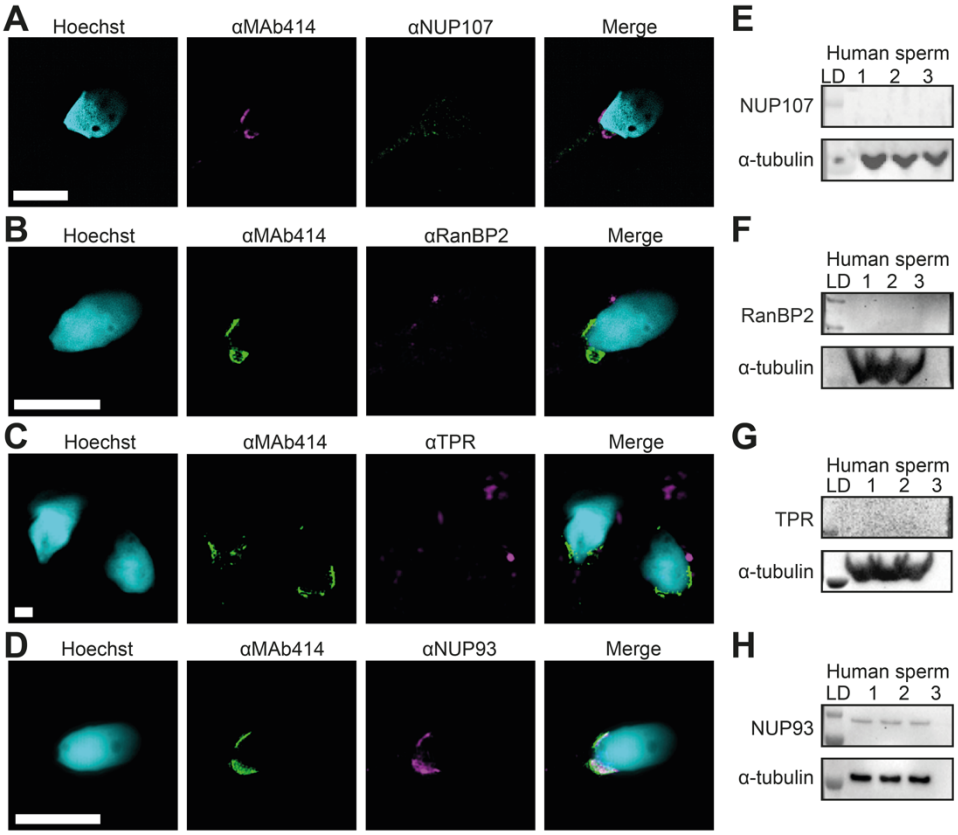

Figure 2 – The CR and the NR are absent from human sperm NPCs. (A-D) SIM imaging of human sperm cells showing localisation of different NPC components, co-immunolabelled with MAb414 in human sperm cells. Scale bars = 1µm **(A)** shows low levels of NUP107 not co-localised with MAb414, **(B)** low levels of RanBP2 not co-localised with MAb414, **(C)** low levels of TPR not co-localised with MAb414, **(D)** NUP93 co-localised with MAb414. **(E-H)** Immunoblots against NPC components **(E)** NUP107; **(F)** RanBP2; **(G)** TPR; and **(H)** NUP93, with replicates, using human sperm lysate and α-tubulin as loading control.

Taken together, our structural, biochemical and imaging data reveal a reduced NPC scaffold architecture in mature human sperm cells, comprising only the IR and displaying a constricted conformation.

Reorganisation of NPCs during human spermatogenesis occurs following meiosis.

To investigate at which stage of human spermatogenesis (Supp Fig. 3A) NPC reorganisation occurs, we performed immunohistochemistry (IHC) on approximately 5µm thick human testicular tissue obtained from five healthy donors. We used MAb414 as a marker for NPCs (Fig. 3A and B; Supp Fig. 3B and C), peanut agglutinin (PNA) for acrosome labelling, and synaptonemal complex protein 3 (SYCP3) for identification of meiotic cells (Supp Fig. 3B and C). We distinguished cells at various differentiation stages according to their radial location in the tissue, their shape and their size. Our data show NPCs distributed uniformly around the NE in pre-meiotic spermatogonia (Fig. 3B, Supp Fig. 3C), similar to somatic cells (Supp Fig. 1B). In cells undergoing meiosis (spermatocytes), MAb414 staining was also distributed around the whole

nucleus, with some NPC-enriched regions, as previously reported using electron microscopy of thin plastic sections[33]. However, following meiosis, NPCs in round spermatids either localised at two opposing poles (Fig. 3B) or at two flanking regions at the rear of the nucleus (Supp Fig. 3C), suggesting that major reorganisation events take place at the final step of meiosis. Following the round spermatid stage, NPCs were observed at their final location at the posterior side of the nucleus in both elongated spermatids and spermatozoa, opposite the acrosomal membrane (Fig. 3B, Supp Fig. 3C).

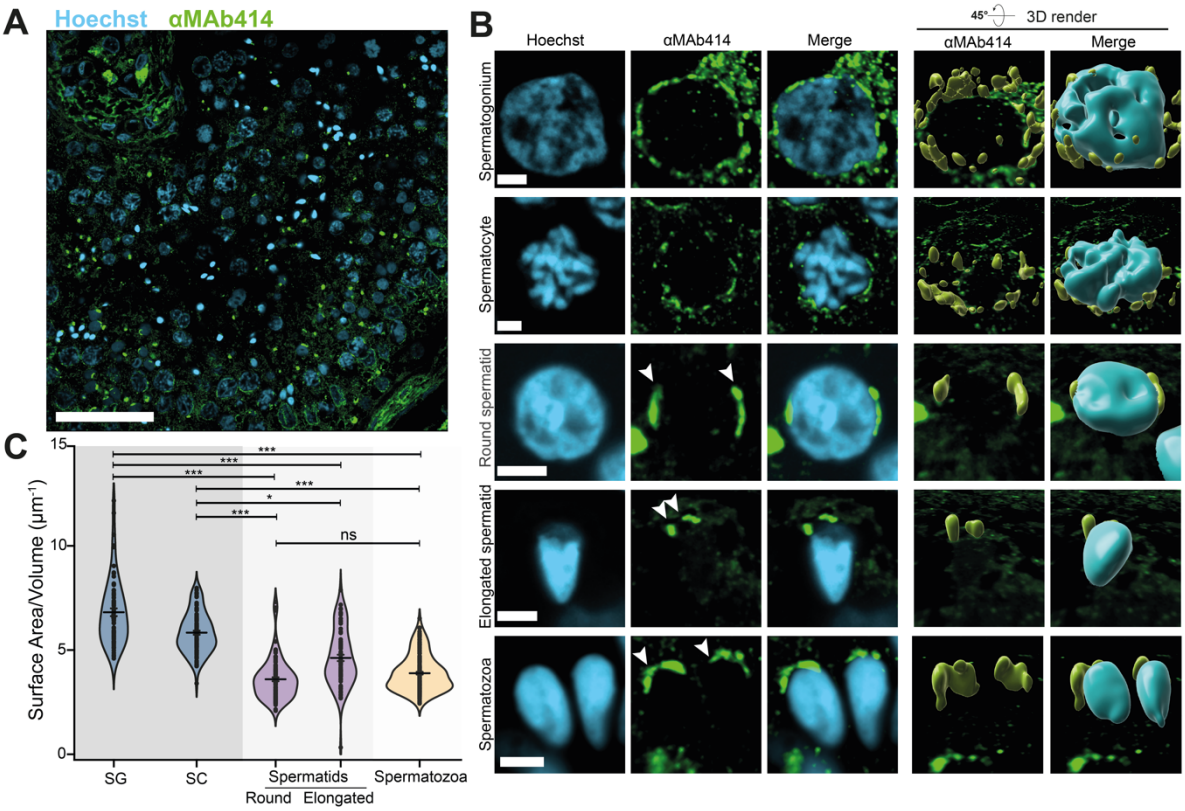

Figure 3 – Re-organisation and clustering of NPCs during human spermatogenesis. (A) Confocal imaging of a seminiferous tubule in testis tissue from a healthy human donor. DNA staining with Hoechst is shown in cyan and NPCs are immunolabelled with MAb414 antibody. Scale bar = 50µm. **(B)** Detail of different cell populations within seminiferous tubules of human testicular tissue, showing distribution of NPCs at the nuclear envelope (NE). 3D rendering of NPC regions and DNA also shown (right panels). Reorganisation of NPCs in post-mitotic cells (arrowheads - round spermatids to spermatozoa) can be observed. Scale bars = 5µm. **(C)** Quantification of surface area/volume ratio of NPC regions for each cell subpopulation in human testicular tissue – spermatogonia (SG), spermatocytes (SC), round and elongated spermatids and spermatozoa. (Mean ± SE values: spermatogonia (SG) = 6.81 ± 0.19 μm^{-1}, n=72; spermatocytes (SC) = 5.83 ± 0.10 μm^{-1}, n=100; round spermatids = 3.60 ± 0.09 μm^{-1}, n=112; elongated spermatids = 4.62 ± 0.15 μm^{-1}, n=80; spermatozoa = 3.89 ± 0.67 μm^{-1}, n=169). Statistical Analysis: ANOVA Tukey test; ns = non-significant = P>0.05; *P<0.05; **P<0.01; *** P<0.001; **** P<0.0001.

To further investigate NPC reorganisation during human spermatogenesis, we performed 3D rendering of our IHC confocal data from human testes sections (Fig. 3B). This allowed us to measure the surface area/volume ratio of MAb414 signal at the NE, as a proxy of NPC clustering (Fig. 3C). Our data show a drop in NPC surface

area/volume ratio from 6.8μm^{-1} in spermatogonia to 5.8μm^{-1} in spermatocytes, and 3.60μm^{-1} in round spermatids, indicating sequential clustering of NPCs (Fig. 3C). However, no significant change was observed between round spermatids and spermatozoa (3.89μm^{-1}). These data suggest that clustering of NPCs is most pronounced during meiosis, and it has largely been achieved by the first stage of spermiogenesis (round spermatid).

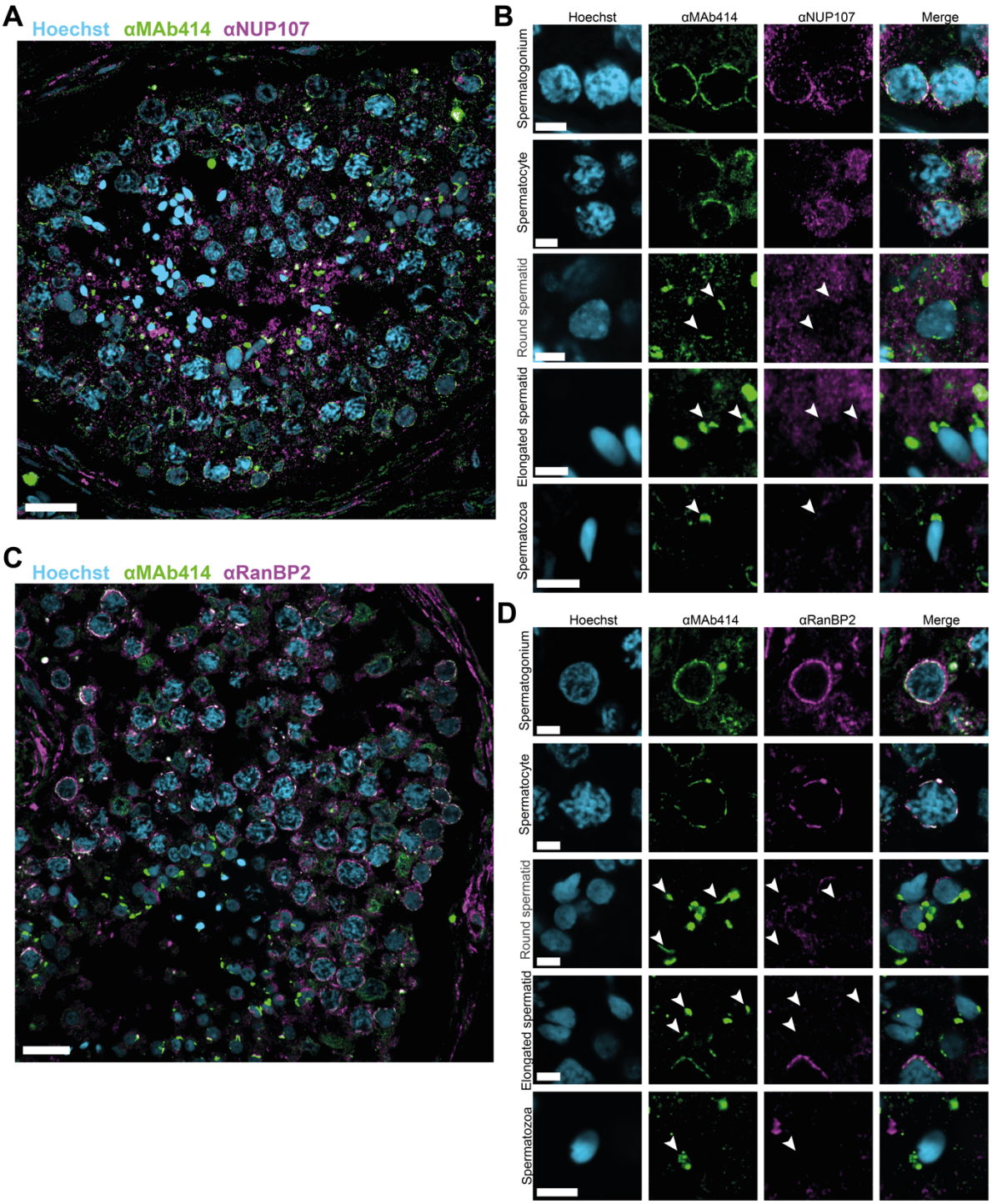

Figure 4 – Absence of outer NPC components in post-meiotic human male germ cells (A) Immunohistochemistry and confocal imaging of a seminiferous tubule from healthy human testis tissue. DNA (Hoechst) is shown in cyan; NPCs (MAb414) in green and Y-complex

component NUP107 is shown in magenta. Scale bar = 50µm. **(B)** Detail of different cell populations within human seminiferous tubules, labelled as described in **(A)** showing re-distribution of NPCs at the NE in green. Arrowheads indicate loss of co-localisation between NUP107 (magenta) and MAb414 during differentiation. Scale bars = 5µm. **(C)** Immunohistochemistry of human testis tissue showing the distribution of NPCs (MAb414, green) and cytoplasmic ring component RanBP2 (magenta) in a seminiferous tubule. DNA stained with Hoechst is shown in cyan. Scale bar = 50µm. **(D)** Sub-populations of differentiating cells labelled as described in (C). Arrowheads indicate loss of co-localisation between RanBP2 and MAb414. Scale bars = 5µm.

To assess at which stage of spermatogenesis the CR and NR are no longer part of the NPC structure, we performed IHC against the Y-complex component NUP107 in human testes (Fig. 4A). NUP107 was present and co-localised with MAb414 at the NE of spermatogonia and spermatocytes (Fig. 4B). However, in post-meiotic cells NUP107 was either absent or no longer localised to either the NE or the NPC regions identifiable with MAb414 (Fig. 4B arrowheads). A similar pattern was observed for RanBP2 (Fig. 4C and D) and TPR (Supp Fig. 3D and E) in tissue: both the proteins co-localised with MAb414 at the NE in spermatogonia and spermatocytes, but co-localisation was lost during spermiogenesis – at round spermatid stage for RanBP2 (Fig. 4C and D arrowheads) and elongated spermatid stage for TPR (Supp Fig. 3D and E arrowheads). Conversely, NUP93 was observed co-localising with MAb414 throughout spermatogenesis and in mature spermatozoa, as expected (Supp Fig. 4A and B).

Interestingly, during reorganisation of NPCs in the human tissue, the presence of strong NPC signal in the cytoplasm of different cell types was also observed. We used calreticulin as an ER marker in human testis sections and often observed co-localisation with the cytoplasmic NPC signal at stages of differentiation between spermatogonia and elongated spermatids (Supp Fig. 4C and D, arrowheads). We postulate that the observed cytoplasmic NPC signal represents annulate lamellae in the tissue[33,55], which are often, but not always, embedded in ER membranes[30].

Altogether these data indicate that changes to both the localisation and structure of NPCs during spermatogenesis occur after meiosis, when germ cells differentiate from spermatocytes to spermatids.

Cryo-ET reveals the presence of filamentous structures embedded between the INM and ONM surrounding NPCs.

Our tomographic analysis showed that NE regions adjacent to NPCs displayed intermembrane distances (distances between the INM and ONM) similar to those observed in somatic cells[69], while these distances were much smaller in regions of the NE further from NPCs (NPC-distal region, Supp Fig. 5A). To quantify this, we performed morphometrics analysis[70] of reconstructed tomograms (Supp Fig. 5A-C). Using these data, we calculated the modal value for each region[70] and show that intermembrane distances significantly decrease from approximately 27nm in NPC-proximal regions to 9nm in NPC-distal regions (Supp Fig. 5B-D).

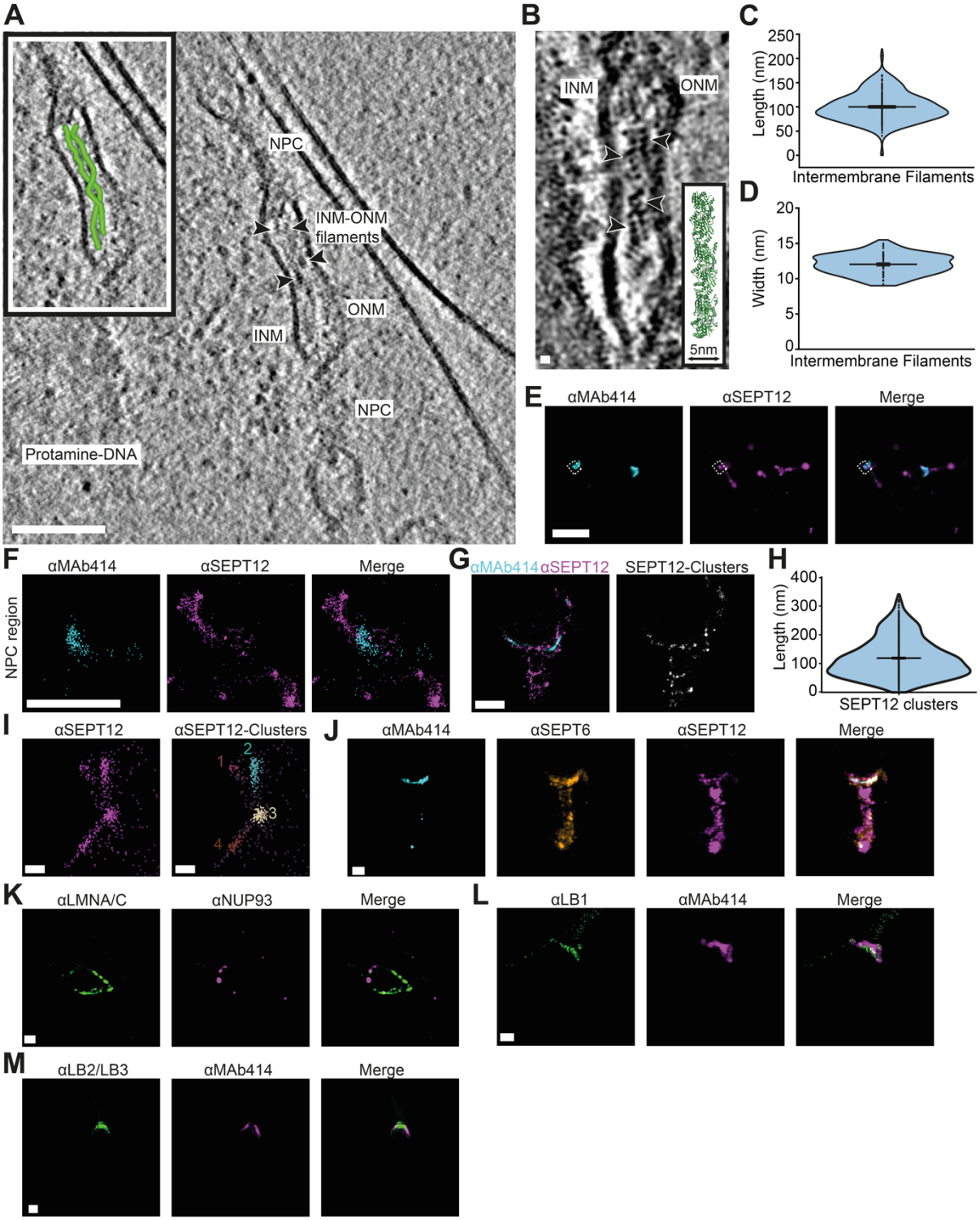

Figure 5 – Filamentous structures within the INM and the ONM space in human sperm cells. **(A)** Tomogram showing the INM and ONM of human sperm cells. Scale bar = 100nm. Arrowheads indicate filamentous structures observed in the INM-ONM space. Segmentation of intermembrane filaments shown in green (top-left corner inset). **(B)** Additional example of nuclear envelope region with intermembrane filamentous structures indicated with arrows showing width of approximately 6.5nm; scale bar = 10nm. Inset detail shows structure of a SEPT2-SEPT6-SEPT7 hetero-oligomer (PDB:9bht). Inset scale bar = 5nm. **(C)** Length measurements of INM-ONM intermembrane filaments calculated from human sperm cryo-ET data. Mean ± SE = 90.9 ± 0.2nm, n = 187 filaments. **(D)** Width measurements of INM-ONM

filaments (dimeric form) from cryo-ET data. Mean ± SE = 12.0 ± 0.2nm, n = 63 filaments. **(E)** Wide-Field imaging of human sperm cells immunofluorescently labelled with SEPT12 (magenta) and MAb414 (cyan). White rectangle shows NPC region selected for super-resolution imaging STORM, shown in (F). Scale bar = 10µm. **(F)** 2-colour STORM of NPC region of the human sperm cell shown in (E). Scale bar = 1µm. **(G)** 2-colour STORM of whole human sperm cell showing SEPT12 (magenta) localisation at the annulus, neck and NPC region co-labelled with MAb414 (cyan). Right panel shows SEPT12 clusters (white) generated with HDBSCAN analysis. Scale bar = 1µm. **(H)** Violin plot showing length measurements of SEPT12 clusters in human sperm cells from STORM data and HDBSCAN analysis. Mean ± SE = 118nm ± 2.5nm, n = 739 clusters **(I)** Zoom-in showing four examples of SEPT12 clusters (numbering 1-4). Left panel shows original STORM data and right panel shows superimposition of clusters detected with HDBSCAN. Scale bar = 100 nm. **(J)** SIM image showing immunofluorescently labelled human sperm NPCs (MAb414, in cyan), SETP12 (magenta) and SEPT6 (orange). Scale bar = 1µm. **(K-M)** SIM imaging of immunofluorescently labelled human sperm cells showing localisation of nuclear lamina components (magenta) LMAN/C **(K)** LB1**(L)** LB2/LB3 **(M)** relative to NPCs (MAb414, green). Scale bars = 1µm.

Analysis of cryo-ET data collected at NPC-proximal regions also revealed filamentous structures within the INM-ONM intermembrane space (Fig. 5A-B; Supp Fig. 5E). These structures were present in all tomograms collected at the NE of NPC-rich regions but absent in NPC-distal regions (Supp Fig. 5A, D and E). Further characterisation and segmentation of the observed densities (Fig. 5A and Supp Fig. 5E) disclosed that they consisted of approximately 90 ± 0.2 nm in length (Fig. 5C) and 6nm width filaments (Fig. 5B). These filaments also displayed a high degree of bending and flexibility and were often found as two intertwined filaments of circa 12nm width (Fig. 5A, B and D, Supp Fig. 5E, Supp Movie 2). Based on these data, we excluded actin filaments, microtubules, lamins, vimentin and other cytoplasmic intermediate filaments[71,72] as possible sources for our filamentous structures.

Previous work on mammalian sperm highlights the importance of septins - polymerising GTP-binding proteins - in spermatogenesis and male fertility[73,74]. For example, septin 12 (SEPT12) is expressed exclusively in testes and specific mutations or changes in its expression levels lead to infertility due to defects in the sperm annulus, or nuclear damage and maturation arrest at the spermatid stage[74-79]. In sperm, SEPT12 has also been shown to interact with NE proteins, including Lamin B1 (LB1), B2/B3 (LB2/3)[80,81], and NDC1[59], a membrane component of the NPC. Additionally, structural characterisation of septins shows their organisation as approximately 5nm-wide single filaments[82,83] (Fig. 5A inset), and 11nm intertwined filaments[84] corresponding to the dimensions of the filamentous densities at NPC-rich regions in our tomograms (Fig. 5A, B and D, Supp Fig. 5E). Therefore, we considered SEPT12 as a plausible candidate to investigate the nature of the observed intermembrane filaments.

Firstly, we performed immunoblotting against SEPT12 confirming, as expected, its presence in human sperm lysate as expected (Supp Fig. 5F). Previous studies show localisation of SEPT12 at the neck and annulus of human sperm cells[74,75,79]. However, our wide-field immunofluorescence data showed SEPT12 signal also extending its localisation to the NPC-proximal region of the NE (Fig. 5E). To obtain higher resolution detail of SEPT12 organisation in this region, we performed STORM. STORM imaging revealed SEPT12 co-localised to NPCs immunolabelled with MAb414 (Fig. 5F and G),

consistent with our cryo-ET data(Fig. 5A and Supp Fig. 5E). Next, we performed quantitative HDBSCAN[85] analysis on SEPT12 STORM data to measure the length of SEPT12 filaments (Fig. 5G-I). From SEPT12 clusters identified by HDBSCAN (Fig. 5I), we could determine that SEPT12 forms elongated clusters with a mean length of 118 ± 2.5 nm (Fig. 5H). These measurements were similar to the ones obtained from cryo-ET data (Fig. 5C) and the discrepancy might be explained by the lower resolution of STORM data (approx. 40nm) and the additional presence of antibodies.

Septins have been reported to form both homo and hetero-oligomers with other septin isoforms[82,86]. In sperm, SEPT12-SEPT7-SEPT6-SEPT2 and SEPT12-SEPT7-SEPT6-SEPT4 hetero-oligomers have been hypothesised based on co-immunoprecipitation studies and due to their co-localisation at the neck and annulus regions[87]. To investigate the possibility of having septin isoforms at the NE of NPC-rich regions, we used immunoblotting to confirm the presence of SEPT6 in human sperm lysate (Supp Fig. 5F) and performed SIM on immunofluorescently labelled human sperm cells. Our imaging data show, as expected, the co-localisation of SEPT6 and SEPT12 in the neck and annulus of sperm cells, but also at the NPC region (Fig. 5J). Higher-resolution imaging with STORM also showed partial co-localisation of SEPT6 and SEPT12 in human sperm cells, including at the NPC region (Supp Fig. 5G and H), suggesting that mixed populations of SEPT12 hetero- and homo-oligomers might be present at the NPC-rich NE regions, which also confirms the previously described heterogeneity of septin filaments[82,86,87].

As previously mentioned, interactions between SEPT12 and lamin isoforms have been reported in sperm cells. We also found the presence of lamin isoforms in NPC-proximal regions of our reconstructed tomograms (Supp Fig. 6A). Immunoblotting of sperm lysates against LB1, LB2 and Lamin A/C (LMNA/C) confirmed their presence in human sperm (Supp Fig. 6B). To investigate the cellular localisation of the different lamin isoforms, we performed immunofluorescence labelling, coupled to SIM imaging in human sperm cells. Both LB1 and LB2/LB3 could be observed at the rear of the nucleus, co-localising with MAb414 (Fig. 5L and M). Conversely, LMNA/C appeared distributed around the whole NE (Fig. 5K).

Overall, based on our data, we propose that the filaments found within the INM-ONM space are homo- and hetero-oligomers of septin isoforms.

Nuclear transport is perturbed in human sperm cells

Our *in-situ* reconstruction of the human sperm NPC revealed large architectural changes, including the absence of the CR and NRs, and a highly constricted central channel. To understand how these changes affect NPC function, we investigated potential disruptions to Ran-dependent active transport and nuclear diffusion into the nucleus.

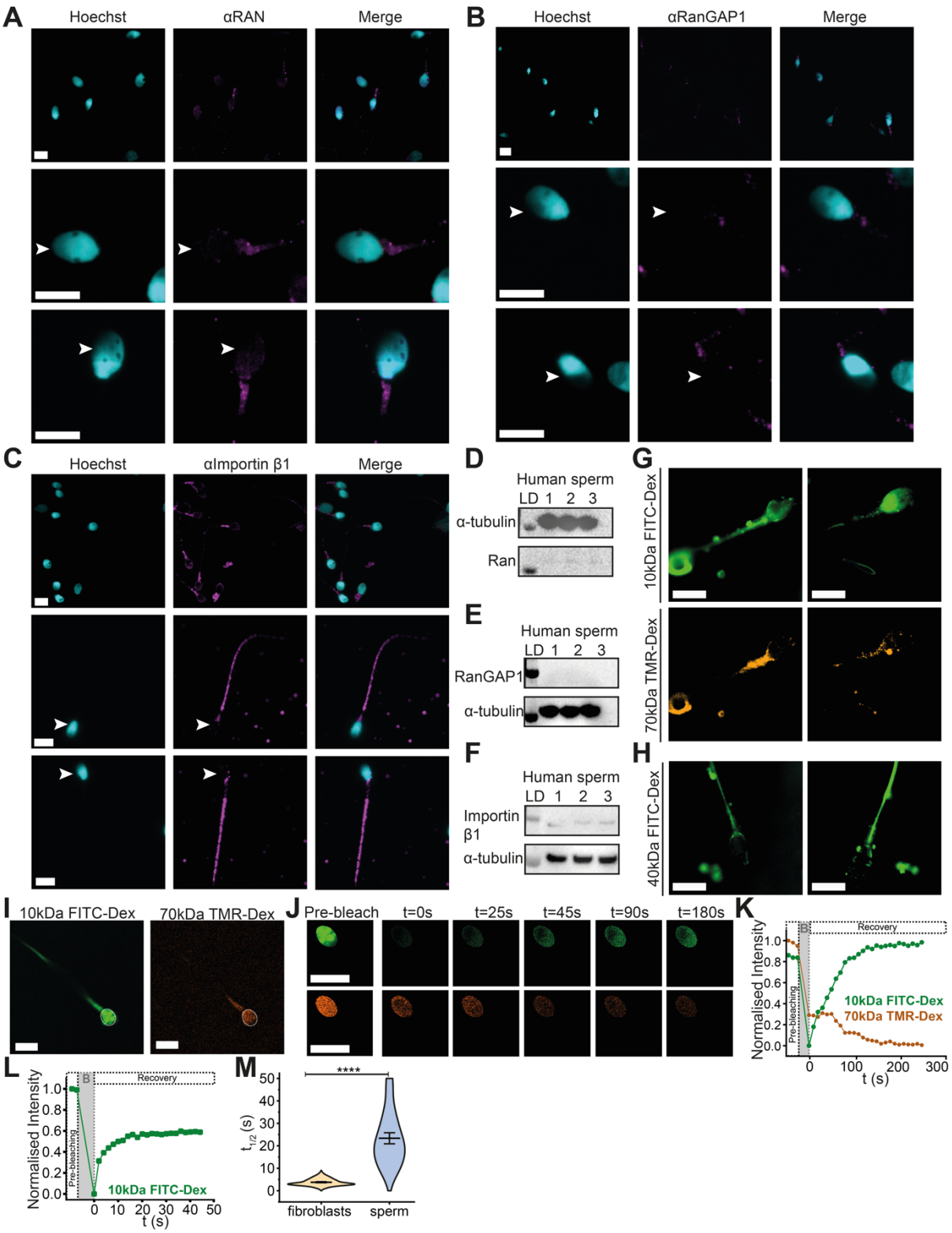

Figure 6 – Nuclear active transport in human sperm is perturbed and passive diffusion is slowed down. (A) Immunofluorescence labelling of human sperm cells showing low levels of Ran localised to the tail and neck. Scale bar = 5µm. **(B)** Immunofluorescence labelling of human sperm cells showing very low abundance of RanGAP1. Scale bar = 5µm. **(C)** Sperm cells immunolabelled with Importin β1 antibody show low amounts of the protein and localisation to tail and neck region. Scale bar = 5µm. **(D-F)** Western blots against Ran **(D)**, RanGAP1**(E)** and Importin β1**(F)** using human sperm lysate. α-tubulin used as loading control and three replicates are shown. **(G-H)** Diffusion test in human sperm cells using digitonin for the delivery of

fluorescently labelled dextrans of different molecular weights. Scale bars = 5µm. **(G)** Two human sperm cells with both 10kDa-FITC Dextran and 70kDa-TMR Dextran showing exclusive passive diffusion of only 10kDa dextran to the nucleus after digitonin treatment. **(H)** Human sperm cells showing inability of 40kDa-FITC dextran to passively diffuse into the nucleus, following digitonin treatment. **(I)** Sperm cell showing even distribution of 10kDa-FITC and 70kDa-TMR dextrans following electroporation. Scale bars = 5µm. Bleaching region used for Fluorescence Recovery After Photobleaching (FRAP) shown as a white-dotted circle. **(J)** Fluorescent images showing the recovery time-course for the cell shown in (I). Scale bars = 5µm. **(K)** FRAP recovery curve for both 10kDa-FITC and 70kDa-TMR Dextran in cell showing in (I and J). **(L)** Example of a recovery curve for a human fibroblast electroporated with 10kDa FITC dextran. **(M)** Calculated half times of recovery ($t_{1/2}$) for 10kDa-FITC FRAP experiments in human fibroblasts and human sperm cells. Mean ± SE: $t_{1/2}$(fibroblasts) = 3.8 ± 0.2s, n = 50 cells; $t_{1/2}$(sperm)=23.4 ± 2.6s, n = 23 cells. Statistical Analysis: t- test; ns = non-significant = P>0.05; *P<0.05; **P<0.01; *** P<0.001; **** P<0.0001.

The maintenance of a Ran-gradient in the cell depends on several factors, including RanGAP1, the Ran GTPase activating protein, which is mostly localised on the cytoplasm and at the outer surface of the NE of mammalian somatic cells[88,89] (Supp Fig. 7B). We investigated the presence and localisation of both Ran and RanGAP1 in human sperm using immunofluorescence and immunoblotting. We detected low levels of Ran almost exclusively localised to the neck and cytoplasmic region of sperm cells[54] (Fig. 6A and D). This differs to its localisation human fibroblasts, where Ran was located at the nucleus during interphase (Supp Fig. 7A and D). Conversely, we could not detect RanGAP1 through immunoblotting in sperm lysates, and immunofluorescence data showed very low signal (Fig. 6B and E) in comparison to fibroblasts (Supp Fig. 7B and E). We then tested the presence and localisation of the main transport receptor importin **β**1. In human fibroblasts, as expected, importin **β**1 was present and mostly nuclear (Supp Fig. 7C and F), whilst in human sperm cells, we detected only small levels of importin **β**1[53,54] (Fig. 6C and F), localised exclusively outside the nucleus at the neck region (Fig. 6C). Taken together, these data point towards a disrupted active transport in human sperm cells.

Previous *in-situ* structural work in *S. pombe* showed that NPC constriction, following hyperosmotic shock, can affect passive diffusion rates of small proteins into the nucleus[40]. As our cryo-ET data showed a highly constricted NPC (Fig. 1D and F, Supp Fig. 1G), with a central channel volume approximately 50% smaller than in somatic cells[39], we also tested this hypothesis. For this, we treated sperm cells with digitonin, as it can permeabilise the cytoplasmic, but not the nuclear membrane of mammalian cells, to deliver fluorescently labelled dextrans of different molecular weights (10kDa, 40kDa and 70kDa). We detected 10kDa-FITC Dextrans in the sperm nucleus due to passive diffusion, but we could not detect the presence of 40kDa-FITC or 70kDa-TMR dextrans in the nucleus (Fig. 6G and H). The same was observed in human fibroblasts (Supp Fig. 7G-I).

After ascertaining that 10kDa dextrans could freely diffuse into the nucleus of sperm cells, we compared passive diffusion rates between human sperm cells and fibroblasts using Fluorescence Recovery After Photobleaching (FRAP). First, we electroporated human sperm cells with both 10kDa-FITC and 70kDa-TMR dextrans to deliver both fluorescent molecules to the whole cell, including the nucleus (Fig. 6I). Then, following bleaching of both fluorophores in the nuclear region, we were able to observe

fluorescence recovery of 10kDa-FITC but not 70kDa-TMR dextran, as expected; indicative that the nuclear membrane remains intact after electroporation (Fig. 6J and K). We then used 10kDa-FITC dextrans for all passive diffusion measurements in sperm cells and fibroblasts (Fig. 6M-N). Our FRAP measurements in human sperm cells displayed higher variability and a large increase in half-time of recovery, relative to human fibroblasts (mean ± SE: sperm $t_{1/2}$= 23.4 ± 2.5 s; fibroblasts $t_{1/2}$= 3.8 ± 0.2s; Fig. 6N). Although other variables might also contribute to this large reduction in passive diffusion rates in sperm cells, we hypothesise that the observed NPC constriction is one of the main causes of this[40].

Overall, our data suggest a direct link between the reduced, constricted NPC architecture and perturbation of both Ran-dependent active transport and passive diffusion to the nucleus in human sperm cells (Fig. 7).

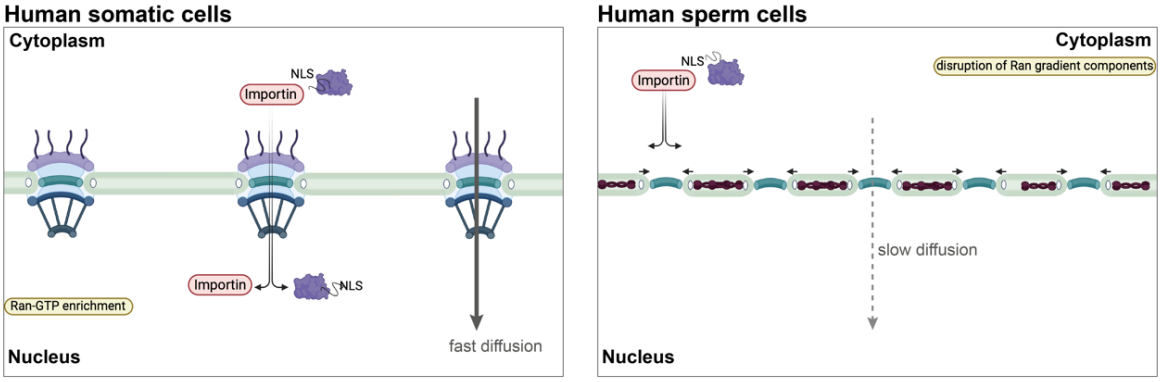

Figure 7 – Structural and functional changes to the NPC of human sperm cells. Human sperm NPCs have a reduced scaffolding, showing absence of the Y-complexes and outer rings, and a highly constricted central channel (indicated by arrows, right panel). These structural changes result in slow passive diffusion of small molecules into the nucleus and in perturbations to the Ran-dependent active transport.

Discussion

In the last decades, specific roles of NPCs in tissue development and differentiation have been revealed[58]. Despite this, structural data are lacking behind. In this study, we investigated the architecture of the human sperm NPC using an integrative *in-situ* structural biology approach. We describe major changes to the NPC structure in human sperm cells, relative to somatic cells[13], including loss of the outer rings (CR and NR), and a high degree of constriction of the central channel (Fig. 1, Fig. 2, Supp Fig. 1, Supp Fig. 2).

In somatic cells, Y-complexes are one of the main scaffold components for the assembly of NPCs[8,90]. However, densities for the Y-complex were not found in our *in situ* structural model (Fig. 1D, Supp Fig. 1D, E and G, Supp movie 1). Consistent with this, we could not detect the Y-complex subunit NUP107 in human sperm lysates through immunoblotting, and immunofluorescence revealed only very low signal not localised at NPCs (Fig. 2A and E). Our data are further validated by two previous proteomics studies[91,92] that did not detect NUP107 in mature human sperm. Despite the absence of the Y-complex, NPCs are highly clustered at the caudal region of the NE (Fig. 1A and B, Supp Fig. 1C, Fig. 3B), with an approximately 7-fold increase in

NPC density, relative to previously reported values for human somatic cells[64-66] (Fig. 1E).

Our human tissue data show that NPC clustering is most pronounced as cells exit meiosis and enter spermiogenesis. In round spermatids, NPCs no longer uniformly decorated the nucleus as they did in spermatogonia, but localised exclusively at two opposing lateral poles (Fig. 3B, Supp Fig. 3C). This is consistent with previous evidence from electron microscopy images of thin plastic sections in rodents and humans, showing accumulation of NPCs at the caudal end of the nucleus of late-stage spermatids[33,55,56]. It is possible that clustering of NPCs at the NE reaches its maximum at the exit of meiosis and for the remaining steps of spermiogenesis nuclear membranes enriched with NPCs descend to the caudal region of the head. Further studies are needed to understand how relocation of NPCs occurs during cell differentiation in testes, but biochemical evidence suggests a microtubule-dependent movement through interactions between NPCs and the kinesin molecular motor KIFC1 during rat spermiogenesis[93]. Investigating this process in the context of human spermatogenesis remains particularly challenging due to tissue sample availability and the impossibility of genetic manipulations.

Our tissue imaging data further indicate that the structural loss of the outer NPC rings occurs at the exit of meiosis, concurrently with NPC clustering. In human testes, we observed co-localisation of the Y-complex component NUP107 and MAb414 in both spermatogonia and spermatocytes, but this was lost in round spermatids (Fig. 4A and B). RanBP2, usually at the CR, was also no longer found to co-localise with MAb414 in round spermatids and the signal was mostly lost in elongated spermatids and spermatozoa (Fig. 4C and D). Similarly, TPR, a nuclear basket component, lost co-localisation with NPCs at the elongated spermatid stage (Supp Fig. 3D and E). Previous work showing the absence of NUP153, another nuclear basket component, in the testis of adult mice where mature spermatozoa are the most abundant species[93], also supports our observations. Future *in-situ* cryo-ET studies in human tissue will add valuable knowledge to the changes in the structure of human NPCs in germ cells at different differentiation stages. Interestingly, NUP107, RanBP2 and NUP153 are present in oocytes[30], suggesting possible complementary roles of NPC components post-fertilisation. Pre-assembled IRs delivered by the sperm cell during fertilisation may facilitate reincorporation of the remaining nucleoporins[14,15,43,94], and these may aid male pronuclear movement[61,62].

Another major finding of this study, enabled by *in situ* cryo-ET, was the observation of filamentous structures embedded in the nuclear intermembrane space between the INM and ONM (Fig. 5A-J, Supp Fig. 5E-H, Supp movie 2). We propose that these filaments are oligomeric forms of septins, in particular of SEPT12 and SEPT6 – a testis and lymphocyte-specific isoform[74,83] (Fig. 5E-J, Supp Fig. 5E-H). SEPT12 is essential for successful spermatogenesis, and its depletion or mutation is known to cause defects in sperm cell morphology and lead to infertility[74-79,87]. However, it is not clear what its specific role during differentiation is. In somatic cells, the role of septins is also not well understood, but evidence suggests they form non-polar filaments that interact with phospholipids and restrict diffusion of membrane-bound proteins[83,84,95,96]. Septins are also thought to have a role in maintaining cell cortex rigidity at specific sites and in subcellular compartmentalisation[97,98]. Previous studies in sperm cells show that SEPT12 interacts with different NE components. These include lamins (LB2/LB3,

LB1), LINC component SUN4, and NDC1[59,80,99] – a membrane component of the NPC. Although previous reports only detected SEPT12 at the annulus and neck of sperm cells[59,75,80,87], our super-resolution imaging data showed its presence extending to NPC regions (Fig. 5F-I, Supp Fig. 5G and H), in agreement with the location of these filaments in cryo-ET data. Our observation is also more in line with the localisation of known NE interactors of SEPT12, including NDC1, and LB1, LB2/LB3, which we show as being present at the INM side of NPC-rich regions (Fig. 5K-M, Supp Fig. 6).

SEPT12 oligomerisation at the NE will, most likely, affect the local mechanics of the membrane[84,98]. This is important, as NPC dynamics respond to local forces altering membrane tension, such as cytoskeletal filaments acting on the NE[40,41,44,46,100]. Our *in-situ* model for the sperm NPC shows a highly constricted central channel. Indeed, the observed central channel diameter was measured at ≤40nm, compared to approximately 55-60nm in human somatic cells (Fig. 1D, Supp Fig. 1G). Lack of scaffold NUPs should lead to loss of structural rigidity of NPCs and translate into the expansion of the central channel, as previously observed[39,40,44]. Our reduced NPC structure is, instead, constricted. We propose that this is the result of forces introduced by the presence of the septins network observed between the INM and ONM. Septin filaments are known to be important in stabilising membranes, by introducing additional rigidity[83,97,98]. As a result, they may prevent NE instability or rupturing during sperm cell movement or fertilisation. Further studies on the role of septins in sperm cells are required to answer these questions.

We also propose that functional changes accompany the structural differences observed in the sperm NPC. For example, RanBP2, crucial for mRNA export[101] and nuclear import[27], largely loss co-localisation with MAb414 in tissue following meiosis and could not be detected in mature sperm (Fig. 4C and D). Similarly, the absence of basket NUPs could affect nucleocytoplasmic transport by changing the availability of docking sites for transport receptors[102-104]. In line with this, we show that in mature sperm cells, the Ran activator protein, RanGAP1, also interactor of RanBP2[27,88,89,105], could not be detected using immunoblotting (Fig. 6E) and immunofluorescence showed very low signal at the tail (Fig. 6B). Additionally, whilst we detected the presence of low levels of Ran and Importin **β**1, we also show their enrichment in the sperm tail, contrasting somatic cells, where the signal is nuclear[24,25,106] (Fig. 6A, C, D and F and Supp Fig. 7A, C, D and F). Ran, in particular, was localised to the centrosomal neck region (Fig. 6A), which supports its proposed function in microtubule assembly, as previously reported in rat spermatids[107]. In addition, our structural data also show absence of nuclear basket signal and only low levels of TPR, not colocalised with MAb414, were observed in immunostaining of human sperm cells (Fig. 1D, Fig. 2D and G, Supp Fig. 1D, E and G Supp Fig. 2G). An exclusively cytoplasmic Importin **β**1 would in fact prevent the import of TPR or NUP153 into the nucleus[108,109], and simultaneously, the unavailability of nuclear basket components would disrupt Importin **β**1-mediated transport[19]. Hence, overall, we accumulated evidence that suggests the perturbation of Ran-dependent active transport in human sperm cells.

Due to the large reduction in the NPC central channel diameter in sperm cells (Fig. 1D and F, Supp Fig. 1E and G), we also hypothesised that there would be changes in nuclear passive diffusion rates. *In situ* structural work of the *S. pombe* NPC[40] has previously shown a strong correlation between NPC diameter reduction and diffusion rates of small molecules into the nucleus. In agreement with this, our data show an

approximately six-fold increase in half-times of recovery for small fluorescently tagged dextrans in the nucleus of sperm cells, compared to human fibroblasts (Fig. 6I-N).

Overall, our study presents the architecture of the NPC in human sperm cells solved using a state-of-the-art *in-situ* integrative structural biology approach. A reduced and constricted NPC architecture represents a plausible mechanism to limit nuclear transport in differentiated sperm cells, emphasising how NPC compositional variability can allow a variety of functions[23,102,110].
In perspective, specialised cells like sperm cells may have additional compositional and functional rearrangement of macromolecules, and variety of quaternary structures may be a common feature of differentiated human tissues[102].
Finally, we expect cryo-tomography to be pivotal in discovering context-dependent changes in NPC architecture in diverse human cell types or tissues, a phenomenon which underlines the crucial regulatory importance of NPCs in animal development and embryogenesis[58].

Methods

Human sperm and testis tissue samples

Human mature sperm cells were purchased from the European Sperm Bank (https://www.europeanspermbank.com/en) which sent us sperm cells from 25 random healthy men. The samples had been previously processed, tested by the bank according to the requirement of the national competent authorities, GMP and WHO standards, as well as EU directives: 2006/86/EC, 2006/17/EC, 2004/23/EC, 2015/565. Sperm cells were screened for morphology, genetic diseases, blood-borne viruses and motility. Consent to use the samples for research purposes was given to the European Sperm Bank.

Human testis FFPE sections (5-10μm thick) from five different individuals, aged 18-55 years of age and with no history of infertility, were obtained from the Imperial College Healthcare Tissue Bank (Department of Surgery and Cancer). All the experimental procedures were approved by the Imperial College Healthcare Tissue bank (Research Ethics Committee approval numbers: 22/WA/0214; ICHTB HTA license: 12275).
Human sperm straws were thawed to room temperature and used immediately after thawing. Cells were checked for motility under an optical microscope before grid preparation or other experiments.

Vitrification

EM grids (Quantifoil R 1/4 Au 200 mesh, Quantifoil Micro Tools GmbH) were glow discharged with an Edwards S150B glow discharger at 30mA for 45sec on both sides of the grid. Plunge freezing was carried out with a Leica GP2 or with a custom-made manual plunger using a sperm concentration of around $3x10^7$ cells/mL and 3.5μl per grid. In some cases, multiple applications of 3.5μl were used to increase the density of cells per grid square. Blotting time was 6-9 sec and liquid ethane was used as the cryogenic.

Cryo focused ion beam (FIB) milling

CryoFIB was carried out using three different instruments. Manual milling was performed using a Scios cryoFIB/SEM (Thermo Fisher Scientific), and automatic milling using either an Aquilos II cryoFIB/SEM (Thermo Fischer Scientific) or a

Crossbeam 550 (Zeiss GmbH). Milling was performed according to previously published protocols[111,112]. Briefly an inorganic platinum layer (~50nm) was sputter-coated in a Quorum chamber (Scios and Crossbeam 550) or in the main chamber (Aquilos II). Following this, a gas injection system (GIS) was used to cover the cells with a layer of organometallic platinum (Trimethyl [(1,2,3,4,5-ETA.)-1 Methyl-2, 4-Cyclopentadien-1-YL] Platinum) to protect cells from curtaining during milling. A milling angle of 7-8°, relative to the grid's plane, was selected for milling. Milling was carried out stepwise using a staircase pattern (0.5nA, 0.3nA, 0.1nA, 30pA) up to 10µm lamella width and 150nm final lamella thickness.

Tilt series acquisition and tomogram reconstruction

Tilt series were collected on a 300kV Titan Krios G3i transmission electron microscope (Thermo Fisher Scientific) equipped with a Bioquantum energy filter (Gatan) and a K3 direct electron detector (Gatan). Images were acquired with a pixel size of 1.63Å using Serial EM PACE tomo scripts[113] and a dose-symmetric tilt scheme[114] with 3° increments. The total electron dose was 100e/Å^2 with each tilt 3 e/Å^2 split in a movie of 6-12 frames, and defocus -2.5 to -5µm.

All movies were imported into Warp[115] for gain and motion correction, tilt selection, CTF correction. Tomograms were reconstructed after aligning the tilt series with AreTomo[116]; Etomo[117] was also used in difficult cases.

Subtomogram averaging

NPC averaging was performed as described previously[38] with modifications. Specifically, 338 NPC volumes were picked using Imod[117] using two points for each NPC to give them a direction towards the cytoplasm. Model files were converted into a star file for Warp 1.1.0 extraction using a custom script[118]. After extraction at bin 6 (9.78Å/pix) volumes were imported into RELION 3.1[119]. An initial model was obtained with relion_reconstruct and volumes were classified (3 classes, T=1, no alignment) and refined using the RELION pipeline. The resulting NPC map was then split into the eight spokes using napari-subboxer[120] (https://github.com/alisterburt/napari-subboxer) and the resulting ~2600 subvolumes were used for 3D classification to discard bad particles (5 classes, T=1) and consensus refinement. Ellipsoidal masks were created in Dynamo[121] to carry out focused refinement for the cytoplasmic region, the inner ring region, the nucleoplasmic region and the luminal region of the NPC spoke[38]. Using dynamo2m[122] subvolumes were exported to M[123] and refined for 3 sub-iterations using one at a time 'Image warp grid, particle poses, stage angles and volume warp grid'. Final refinements were performed in RELION (Supp. Fig. 1F).
UCSF Chimera was used to visualise maps, to create a composite map of the whole C8 symmetric NPC using Chimera's "*fit-to-map*" for each of the single refined spokes, and to make figures and the Supp movie 1.

Tomogram segmentation and analysis

The nuclear membrane was segmented manually in Imod[117] using Drawing Tools and linear/meshing interpolation. Filaments in the nuclear membrane were traced using Imod (https://www.andrewnoske.com/wiki/IMOD_-_segmenting_tubes) which also computes their length and their width was measured manually. NPC diameters were measured manually in Imod and their density per µm^2 was calculated dividing the total nuclear membrane surface area from 35 tomograms by the NPCs number. NPC central channel volume was estimated using only the IR central channel volume

calculated as a cylinder with a height of 20nm as in[39]. The distance from the inner to the outer nuclear membrane was estimated using surface morphometrics[70].

Cell culture

Human skin fibroblasts derived from AG10803 and immortalised with SV40LT and TERT were a gift from Delphine Larrieu. Cells were cultured in Dulbecco's modified Eagle's medium, supplemented with 10% foetal bovine serum (FBS) and penicillin/streptomycin. Cells were maintained at 37°C, 5% CO_2.

For digitonin experiments, sperm cells or fibroblasts were incubated for 30 minutes with 2μg/mL digitonin and 5μM dextrans (10kDa-FITC, 40kDa-FITC or 70kDa-TMR dextrans) at 37°C, 5%CO_2. Cells were then washed with PBS and allowed to recover for 1h before fixation and imaging.

For Hoechst staining, live cells were incubated for 10min with Hoechst 33342 (ThermoScientific) at 37°C, 5%CO_2 and then washed with PBS before fixation or imaging.

Antibodies

Primary antibodies for NPC components were selected based on their antigenicity to ensure minimal cross-reactivity with other NUPs. For antibody details and dilutions used see supplementary table 1.

Immunofluorescence

Human fibroblasts were seeded on #1.5 glass coverslips for 24h at 37°C, 5% CO_2 before fixation and immunofluorescence procedures. Human sperm cells were spread on #1.5 coverslips pre-functionalised with Poly-L-lysine (PLL) and left at room temperature until dry. Cells were then fixed for 10 minutes at room-temperature (RT) in 4% PFA, then washed in PBS. Samples were quenched with 50mM NH_4Cl in PBS for 15 minutes at RT, followed by washes in PBS. Cells were then permeabilised and blocked in 3% bovine serum albumin (BSA), 0.2% Triton-X100 for 30 minutes at RT. Following this, cells were incubated for 2h at RT with primary antibody diluted in 3% BSA, 0.2% Triton X-100 in PBS. Cells were washed using 0.5% BSA, 0.05% Triton X-100 in PBS and incubated for 1 hour at RT with fluorescently labelled secondary antibodies in 3% BSA, 0.2% Triton X-100 in PBS. Cells were then washed in 0.5% BSA, 0.05% Triton X-100 in PBS, followed by PBS and mounted using Prolong Gold (ThermoFisher). Antibody dilutions are specified in Supp Table 1.

Immunoblotting

Fully-adhered human fibroblasts were washed in PBS and immediately lysed in the tissue culture dish with 1xNUPAGE LDS sample buffer (Invitrogen) supplemented with 50mM DL-Dithiothreitol (DTT), which was then incubated at 95°C for 10 minutes.

Human sperm cells were centrifuged at 300x*g* for 15min at RT. The supernatant was carefully removed, and the pellet was resuspended in an equal volume of 1x NUPAGE LDS Sample buffer (Invitrogen) supplemented with 50 mM DTT and incubated for 10min at 95°C.

Proteins were separated using NUPAGE 4-12% Bis-Tris gels (ThermoFisher) or 3-8% tris-acetate gels (ThermoFisher) and MES SDS or MOPS SDS running buffer. Proteins were transferred onto PVDF membranes (BioRad) for immunoblotting and sequentially incubated in primary antibody solution, washing solution, secondary antibody solution and washing solution using an iBind Flex (ThermoFisher) system

and iBind Flex Solution kit reagents (Invitrogen). Immunoblots were imaged using a BioRad Chemidoc MP. Antibody dilutions are specified in Supp Table 1.

Immunohistochemistry

Glass slides with pre-mounted FFPE-embedded testis sections (5μm thick) from five healthy donors with no history of infertility and between 18-55 years of age were obtained from Imperial College Healthcare Tissue Bank (Research Ethics Committee approval numbers: 22/WA/0214; ICHTB HTA license: 12275).

FFPE sections were deparaffinised, rehydrated and subjected to heat-induced antigen retrieval in 10mM Sodium Citrate, 0.05% Tween 20 (pH6). Tissue sections were then washed in 0.05% Triton-X100 in TBS for 15min with rocking at room temperature, followed by incubation in blocking solution (1%BSA, 10% Donkey Serum in TBS) for 30min at room temperature. Then they incubated with primary antibodies in 1% BSA in TBS, overnight at 4°C. Following this, tissue sections were washed in 0.05% Triton X-100 in TBS, for 10min at room temperature, with rocking, 3 times. Then they were incubated for 1h at room temperature with fluorescently labelled secondary antibodies, diluted in 1% BSA in TBS. Tissue sections were then washed in 0.05% Triton-X100 in TBS, for 10min at room temperature three times, followed by a TBS wash and diH_2O. Tissue sections were stained with Hoechst 33342 (Thermo Scientific) and mounted using #1.5 coverslips and Prolong Gold Mounting media (ThermoFisher). For antibody dilutions refer to Supp Table 1.

Antibodies

Primary antibodies for NPC components were selected based on their antigenicity to ensure minimal cross-reactivity with other NUPs. For antibody details and dilutions used see Supp Table 1.

Fluorescence Recovery After Photobleaching

Cells (both human sperm cells and human fibroblasts) were electroporated with 10kDa-FITC and 70kDa-TMR dextrans using a 4D-Nucleofector X Unit (Lonza) and reagents (Lonza). Following this, cells were let to adhere to μ-Slide 8-well high glass bottom dishes (ibidi) for 24h (human fibroblasts) or for 30min (sperm cells – ibidi surface pre-treated with PLL) at 37°C, 5%CO_2. Cells were then washed in CO_2-independent medium (ThermoFisher) before imaging.

FRAP measurements were performed using a Zeiss LSM780 system, equipped with a heated stage and incubator and a 63x 1.4NA immersion oil objective. Built-in multi-band dichroic mirrors were used to reflect the excitation laser onto the sample. Fluorescent signal was collected using a multi-anode photomultiplier tube (MA-PMT) with 0.96μs pixel-dwell time.

Three frames were acquired under 488 or 561nm wavelength laser illumination before photobleaching. Selected regions of interest were exposed to full laser power, followed by 200 seconds of image acquisition. The time course of fluorescence intensity from the selected regions was recorded by Zeiss Zen 2.3 Blue software. Fluorescence intensity time traces for the regions of interest, whole-cell and background area were analysed using Zeiss Zen 2.3 Blue software (Zeiss). $t_{1/2}$ values were calculated in Zen (Zeiss) by fitting a single-exponential to the normalised data.

Stochastic Optical Reconstruction Microscopy and Cluster Analysis
Following immunofluorescence protocol, cells were imaged using a Nanoimager (ONI) system, with a 100x 1.49NA (TIRF) oil immersion objective. Imaging was performed using 488nm, 561nm and/or 640nm wavelength illumination, with acquisition of 20 000 frames and 30ms exposure time. All STORM imaging was performed using Highly Inclined and Laminated Optical Sheet (HILO) illumination with laser power 60-150mW. Imaging was performed in STORM buffer - 10% glucose, 10 mM NaCl, 50 mM Tris-HCl pH8.0, supplemented with GLOX solution (5.6% glucose oxidase and 3.4 mg/ml catalase in 50 mM NaCl, 10 mM Tris-HCl pH 8.0) and 0.1% 2-mercaptoethanol.

For two colour STORM, channel alignment was performed using a calibration procedure with TetraSpeck beads (Invitrogen). Image processing of STORM data was performed using CODI software (ONI), including drift-correction and HDBSCAN analysis. For HDBSCAN analysis of SEPT12 STORM data, a minimum cluster size was set at 15 molecules.

Structured Illumination Microscopy
Following immunofluorescence protocol, SIM imaging was performed using a Zeiss Elyra S.1 system equipped with a 63x 1.46NA plan-apochromat oil immersion objective; 405nm, 488nm, 561nm and 647nm laser lines and a sCMOS camera. 0.091μm Z-stacks were collected with 5 rotations and frame averaging of 4. Channel alignment was performed using a calibration procedure with the affine method, with mounted TetraSpeck beads (Invitrogen).

Data analysis including channel alignment, deconvolution and SR-SIM post-processing was performed in Zeiss Zen Black 2.3 (Zeiss). 3D SIM reconstructions were performed using Imaris software (Oxford Instruments).

Confocal Microscopy
Tissue sections were imaged using an Andor Bench Top Confocal BC43 (Oxford Instruments), equipped with a 60x 1.42NA oil immersion objective, 405nm, 488nm, 561nm and 638nm lasers. For imaging acquisition Fusion software (Oxford Instruments) was used, and image analysis was performed using Imaris software (Oxford Instruments), including 3D segmentation of cells and rendering.

Data availability
Cryo-EM map of the sperm nuclear pore complex IR has been deposited in the Electron Microscopy Data Bank (EMDB) with the accession code: EMD-51638.

Acknowledgments
We thank the Barford lab members and Victoria Hale for useful discussions and critical feedback. We thank Martin Beck and Bernhard Hampoelz for supporting the early stages of this project. We thank Delphine Larrieu for providing hTERT human skin fibroblasts. We thank Andrew Carter for insightful scientific discussions. We thank the cryo-EM Facility at the LMB for maintaining the electron microscopes, the Scientific Computing facility for maintaining our computer cluster and the Light Microscopy Facility for technical support with light microscopy experiments, in particular Tomás Pais de Azevedo for FRAP experiments. We acknowledge Diamond for access to the Aquilos-II of the UK national electron Bio-Imaging Centre (eBIC), in particular James B. Gilchrist for running the instrument.

This work was supported by the Medical Research Council, as part of United Kingdom Research and Innovation (also known as UK Research and Innovation) [MC_UP_1201/30; MC_UP_1201/6]. For the purpose of open access, the MRC Laboratory of Molecular Biology has applied a CC BY public copyright licence to any Author Accepted Manuscript version arising.
M.A. was funded by the UKRI Medical Research Council (MC_UP_1201/30), A.d.S. was funded by the Wellcome Trust Early Career Award (227622/Z/23/Z), D.Ba. was funded by UKRI/Medical Research Council (MC_UP_1201/6) and Cancer Research UK (C576/A14109).
Human tissue samples used in this research project were obtained from the Imperial College Healthcare Tissue Bank (ICHTB). ICHTB is supported by the National Institute for Health Research (NIHR) Biomedical Research Centre based at Imperial College Healthcare NHS Trust and Imperial College London. ICHTB is approved by Wales REC3 to release human material for research (22/WA/0214).

Author Contributions
M.A. and A.d.S. conceived and designed the experiments; A.d.S. and M.A. wrote the manuscript; A.d.S, M.A., T.D. and G.C. collected cryo-ET data; M.A. and A.d.S. analysed cryo-ET data; A.d.S. performed cryo-FIB milling, immunohistochemistry, STORM, SIM and FRAP experiments; O.K. performed immunoblotting, immunofluorescence and SIM experiments, supervised by A.d.S.; A.d.S performed light microscopy analysis; A.B. and T.D. wrote scripts for tomographic analysis; T.H. performed morphometrics analysis; P.K. supported immunoblotting work and data analysis; D.Be. supported cryo-FIB milling; D.Ba. provided guidance and technical input; M.A. supervised the study.

Declarations of Interests
The authors declare no competing interests.

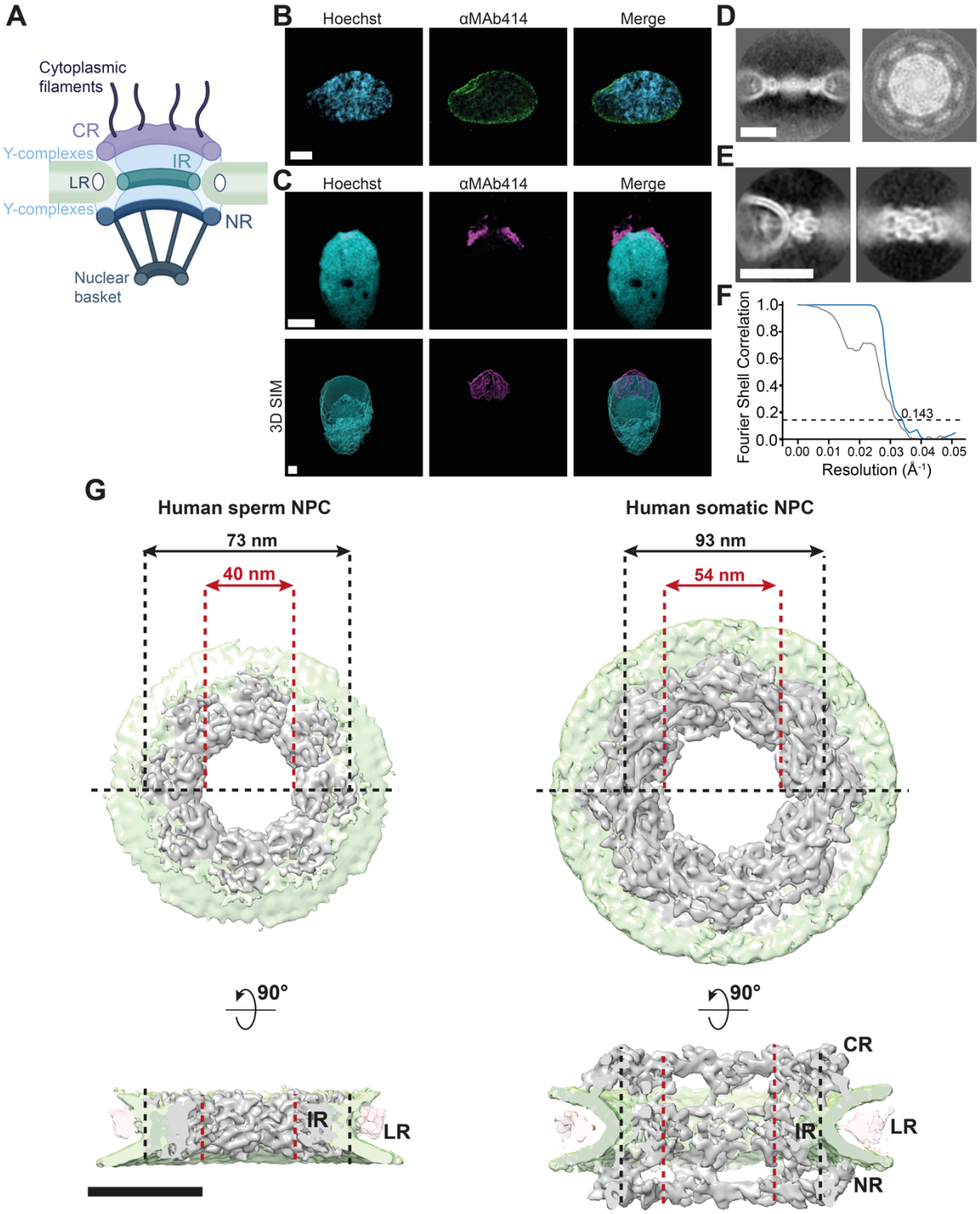

Supplementary Figure 1 – Human Sperm NPCs. (A) NPC Schematic showing canonical three ring organisation: inner ring (IR), nuclear ring (NR) and cytoplasmic ring (CR). Y-complexes, cytoplasmic filaments, nuclear basket and luminal ring (LR) are also shown. **(B)** Distribution of NPCs in human fibroblasts immunolabelled with MAb414 antibody (in green). DNA stained with Hoechst shown in cyan. Scale bar = 5µm. **(C)** Additional examples of 2D and 3D distribution of NPCs in human sperm cells using SIM in cells immunolabelled with MAb414 antibody (magenta). DNA stained with Hoechst shown in cyan. Scale bar = 1µm. **(D)** Subtomogram averaging of whole NPCs *in-situ* from human sperm cells. Scale bar = 50 nm. **(E)** Sub-boxing averages of *in-situ* NPCs from human sperm cells. Scale bar = 50 nm. **(F)** FSC curves for human sperm NPCs *in-situ*. FSC

curve for inner ring shown in blue (~30Å resolution) and for the luminal ring in grey (~35Å resolution). Dotted black line displays 0.143 threshold. **(G)** Comparison between the *in-situ* architecture of the human sperm NPC (this study) and the human somatic NPC structure from HEK cells (EMD-14321[13]). CR, IR and NR are indicated. Central channel diameters (40nm for sperm NPC and 54nm for somatic NPC) are shown with red dashed lines and membrane-to-membrane distance (73nm for human sperm NPC and 93nm for human somatic NPC) shown with black dashed lines. Scale bar = 50nm.

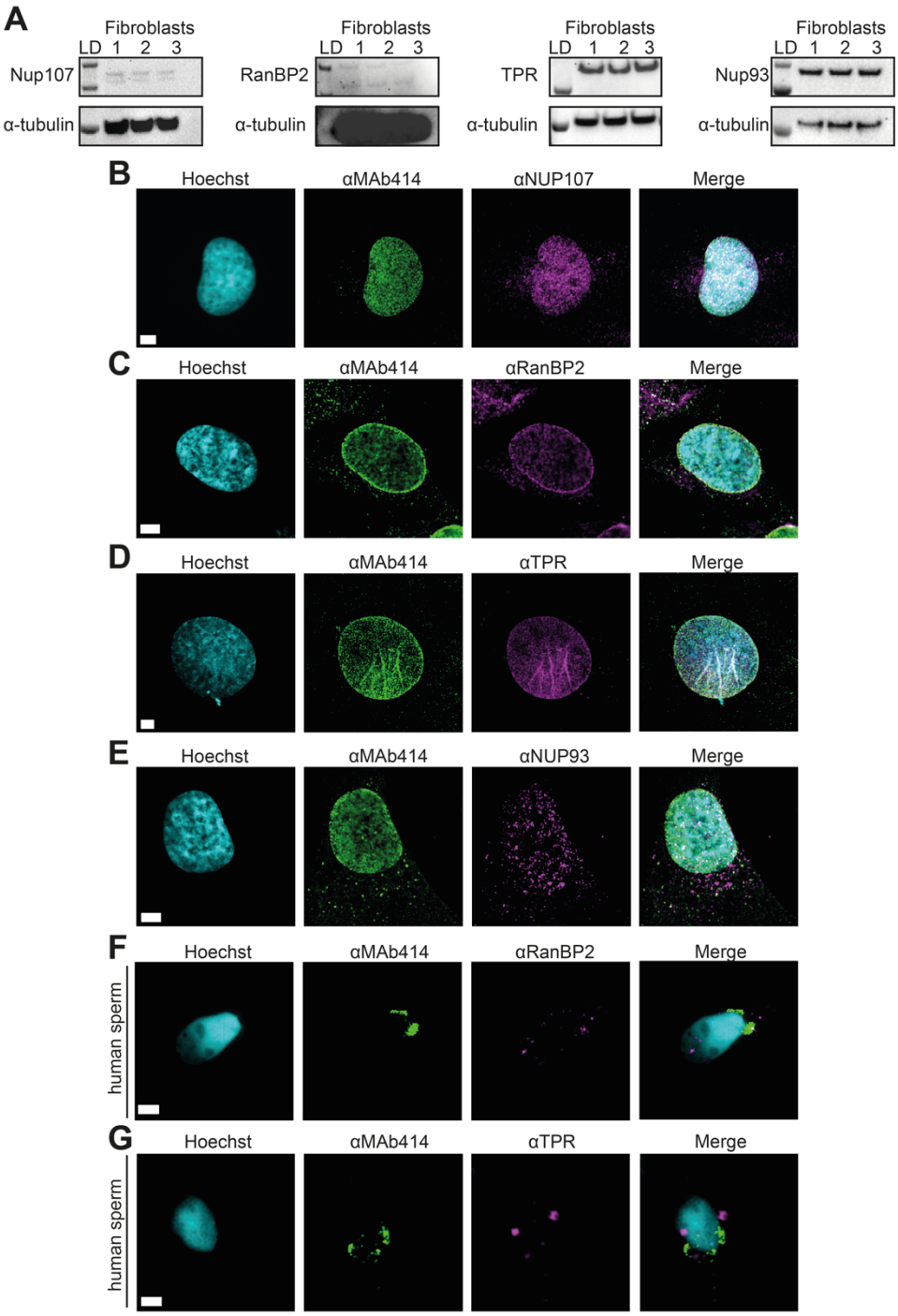

Supplementary Figure 2 – NPC components in human somatic cells. (A) Western blots against NPC components NUP107, RanBP2, TPR and NUP93 using human fibroblasts lysate. (**B-E)** Immunofluorescence and confocal imaging of NPC components in human fibroblasts. Y-

complex component NUP107 **(B)**, CR component RanBP2 **(C)**, nuclear basket component TPR **(D)** and IR component NUP93 **(E)** are shown, with MAb414 antibody. Scale bars = 5µm. **(F and G)** SIM imaging of human sperm cells immunofluorescently labelled with RanBP2 **(F)**, and TPR **(G)**. Cells were co-immunolabelled with MAb414. Hoechst is shown in cyan for DNA labelling. Scale bars = 1µm.

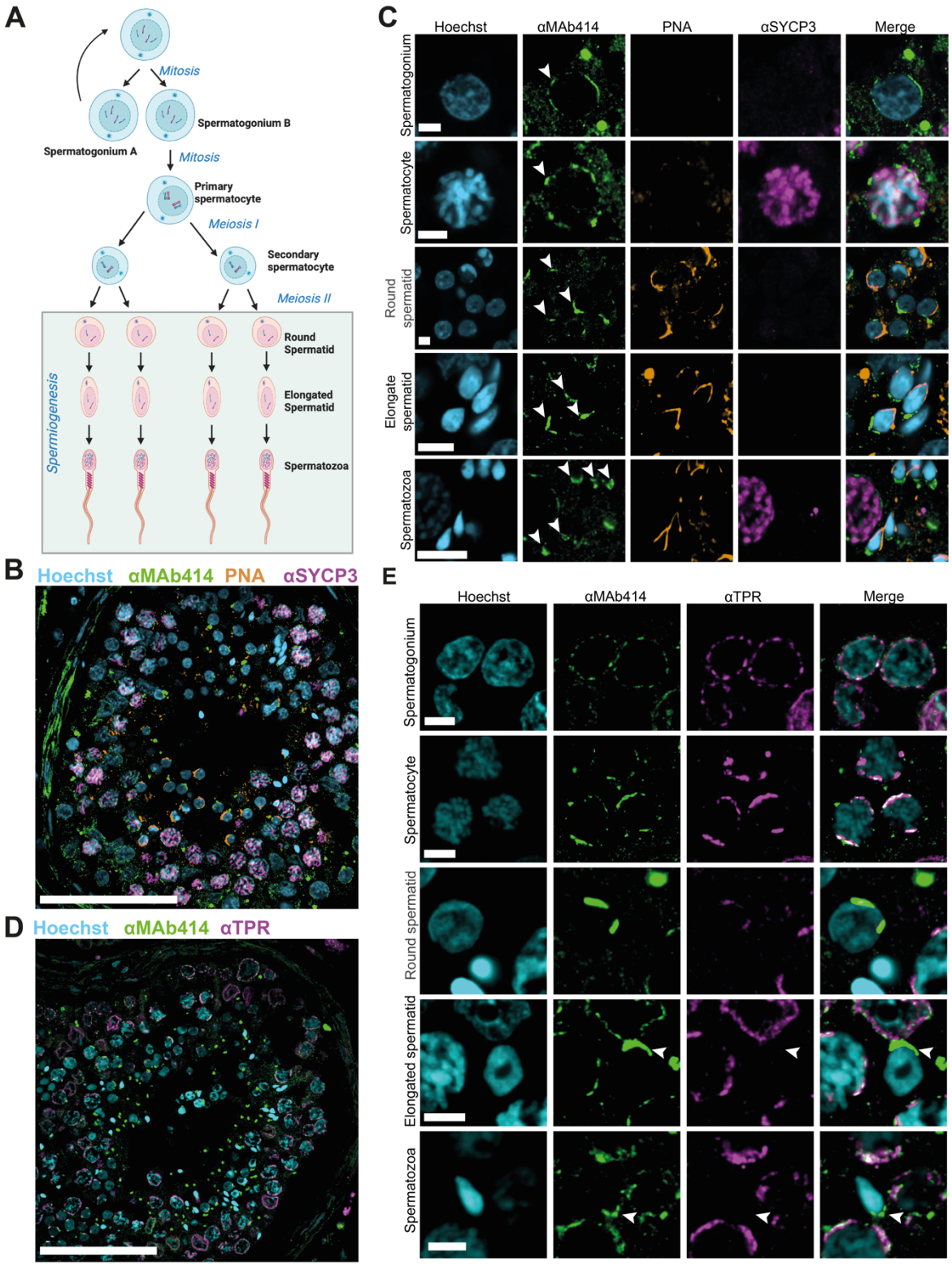

Supplementary Figure 3 – Reorganisation of NPC components during human spermatogenesis. (A) Schematic of sperm cell differentiation in testis (spermatogenesis). Cell

populations are indicated: spermatogonia, spermatocytes, round spermatids, elongated spermatids and spermatozoa. From round spermatid to spermatozoa stage (post-meiotic stage) the differentiation process is referred to as spermiogenesis. **(B)** Confocal imaging of seminiferous tubule from human testis sections, showing NPCs in green (MAb414), DNA stained with Hoechst shown in cyan, meiotic marker SYCP3 and Peanut Agglutinin (PNA) as an acrosomal marker (orange). Scale bar = 50µm. **(C)** Detail of subpopulations of cells labelled as described in **(A)** showing reorganisation of NPCs (arrowheads, green) relative to the acrosome (orange). Hoechst staining of DNA is shown in cyan. Scale bar = 50µm. **(C)** Immunohistochemistry and confocal imaging of human seminiferous tubule. NPCs (MAb414) are shown in green and nuclear basket component TPR is shown in magenta. Scale bar = 50µm. **(D)** Detail of subpopulations of cells in human testes, labelled as described in **(C)**. Arrowheads indicate loss of co-localisation between MAb414 and TPR signals. DNA is shown in cyan (Hoechst). Scale bar = 5µm.

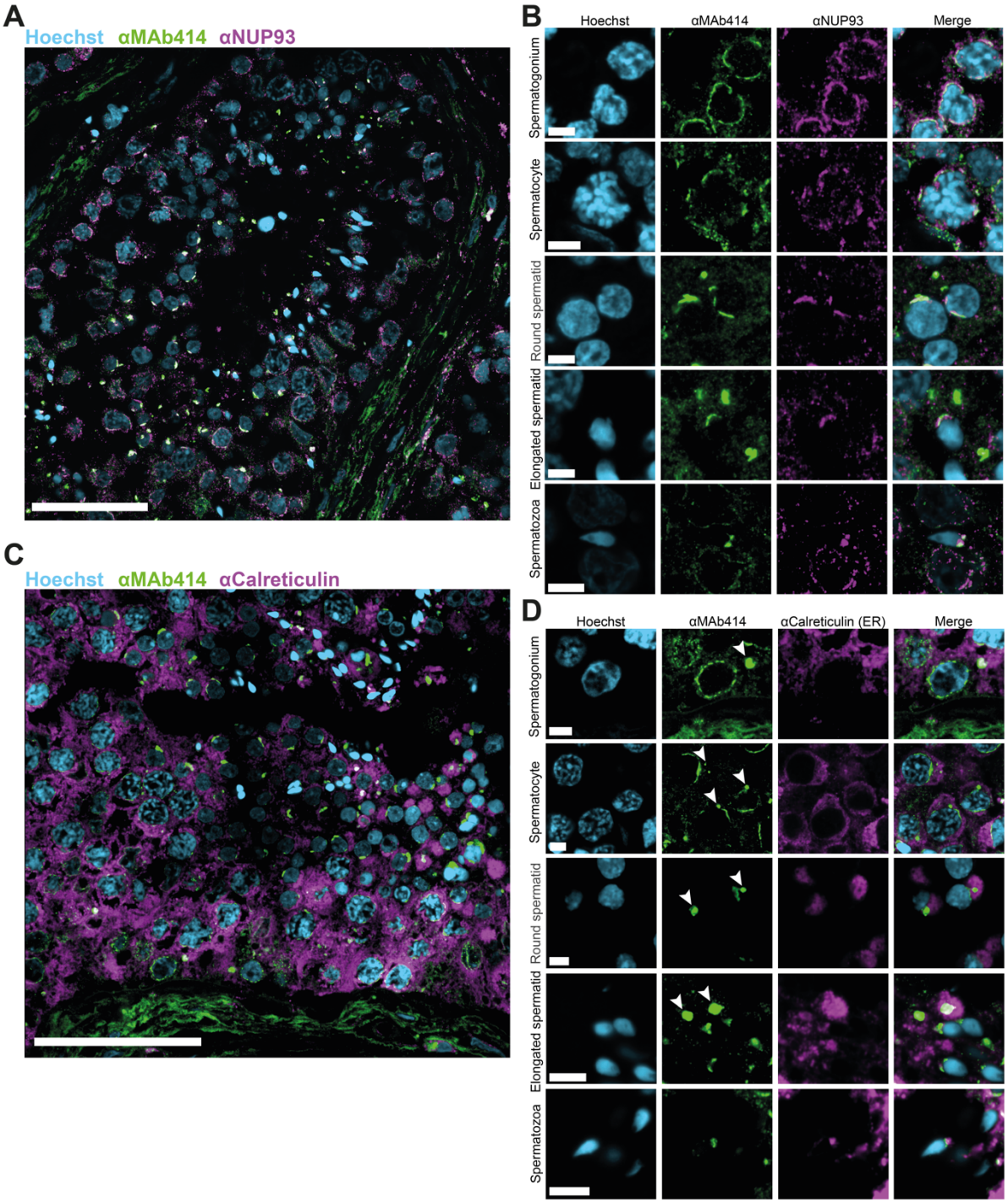

Supplementary Figure 4 - Localisation of NPC components and ER during spermatogenesis. **(A)** Immunohistochemistry and confocal imaging of human seminiferous tubules in testis tissue sections, showing localisation of NPCs (MAb414, green) and IR component NUP93 (magenta). Hoechst is shown in cyan. Scale bar = 50µm. **(B)** Detail of cellular sub-populations in human testis, labelled as described in **(A)** showing co-localisation of MAb414 and NUP93 at all steps of differentiation. **(C)** Overview of human seminiferous tubule following showing endoplasmic reticulum (ER) marker calreticulin in magenta and MAb414 (green). Scale bar = 50µm. **(D)** Detail of differentiating cells in human testis with labelling as described in **(C)**. Arrowheads indicate co-localisation of MAb414 signal (green) and calreticulin (magenta) in the cytoplasm of all cell types, except mature spermatozoa. Scale bar = 5µm.

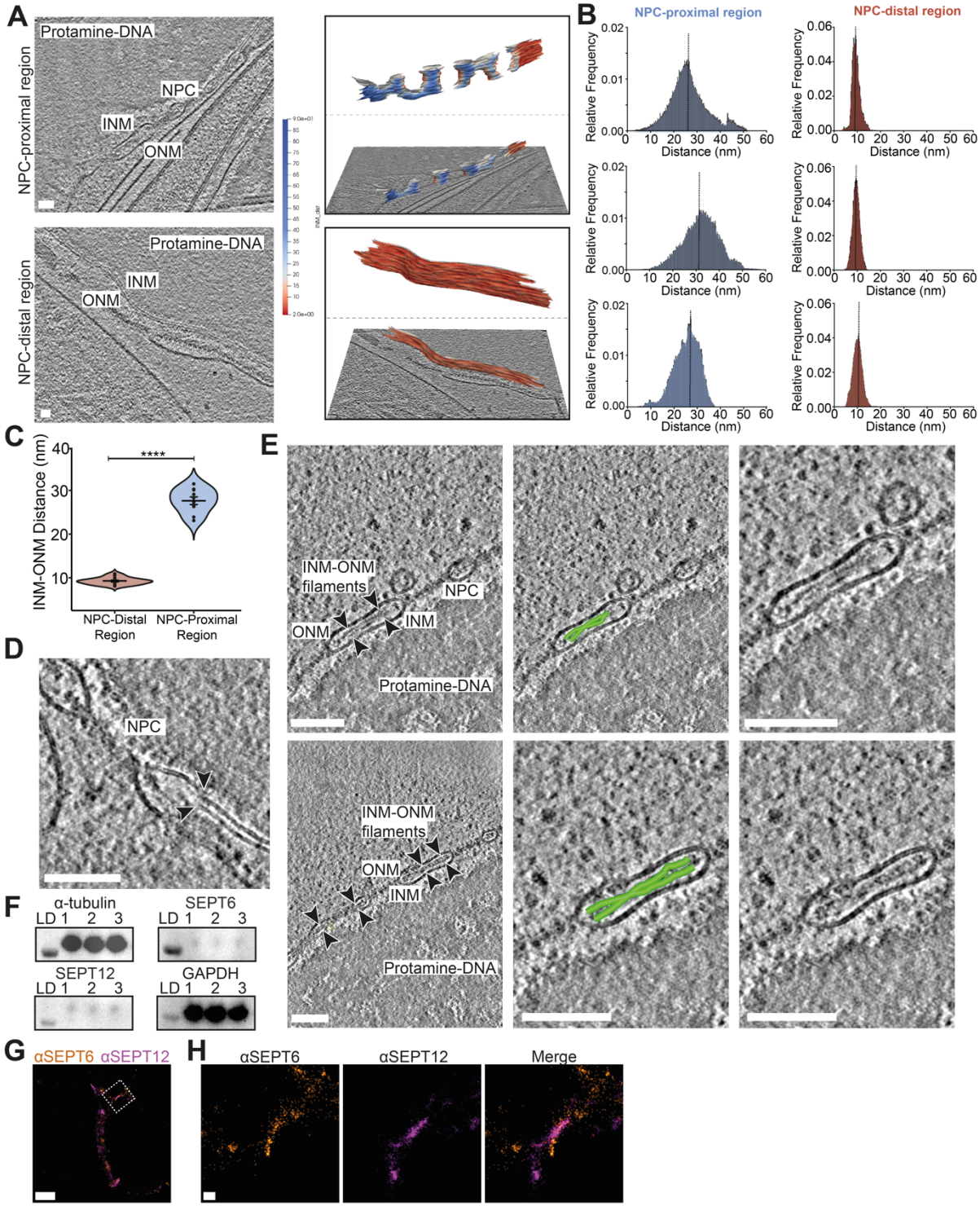

Supplementary Figure 5 – INM-ONM intermembrane filaments. (A) Tomograms showing INM and ONM spacing examples relative to their proximity to NPCs. NPC-distal and proximal regions considered as >200nm and <150nm distance, respectively, from the centre of an NPC. Morphometrics segmentation and heat map of INM-ONM distances shown on the right panel. Blue colour indicates wider INM-ONM distances; brown indicates shorter distances. Scale bars = 100nm. **(B)** Example histograms, plotted from morphometrics analysis of tomographic data, showing distribution of INM-ONM distances. Each histogram represents the distributions of INM-ONM measurements for a single tomogram. Histograms for NPC-distal regions shown in brown, and for NPC-proximal regions in blue. Modal values are shown as black dashed lines. **(C)** Violin plots with distribution of modal values obtained from histograms, following morphometrics

analysis of tomographic data. Mean ± SE values: NPC-distal region = 9.24 ± 0.20nm, n = 16 cells; NPC-proximal region = 27.64 ± 2.76nm, n = 10 cells. Statistical Analysis: t- test; ns = non-significant = P>0.05; *P<0.05; **P<0.01; *** P<0.001; **** P<0.0001.
(D) Tomogram detail of transition region (arrowheads) between narrow INM-ONM and wider INM-ONM regions. Scale bar = 100nm. **(E)** Tomography data of NPC regions in human sperm cells showing the presence of filamentous structures within the INM-ONM intermembrane space (arrowheads). Mid-panel shows tomogram segmentation of filaments, and a zoomed-in image is shown on the right-panel. Scale bars = 100nm. **(F)** Immunoblots for SEPT12 and SEPT6, using human sperm lysate. Replicates and loading controls α-tubulin or GAPDH are shown. **(G)** STORM imaging of a human sperm cell showing localisation of SEPT12 (magenta) and SEPT6 (orange). Dashed white-line rectangle shows detail of an NPC region. Scale bar = 1µm. **(H)** STORM image showing localisation of SEPT12 (magenta) relative to SEPT6 (orange) in NPC region selected from **(H)** – dashed-white rectangle. Scale bar = 100nm.

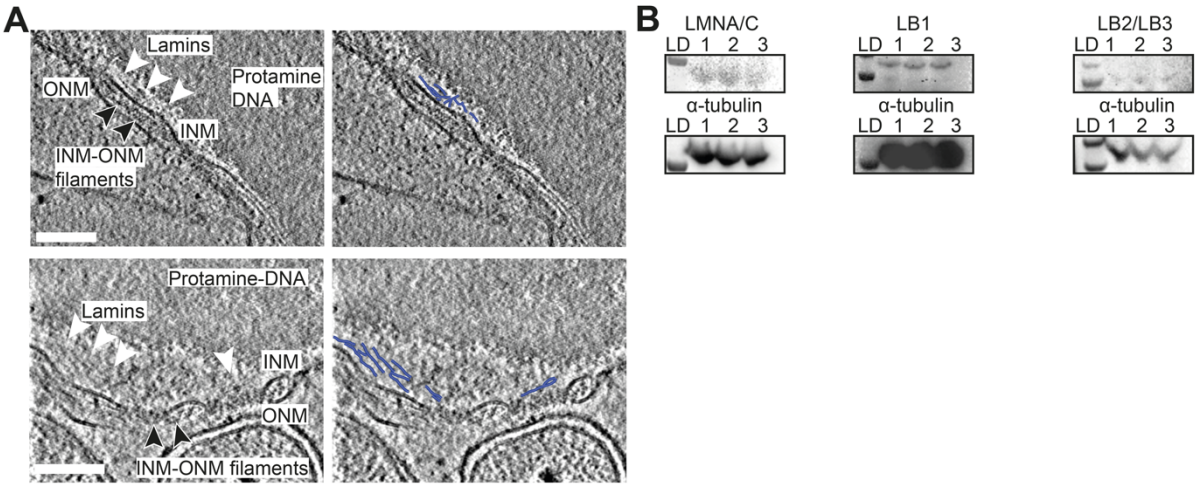

Supplementary Figure 6 – Lamins in human sperm cells. (A) Observation of nuclear lamina (white arrowheads) at the NE of human sperm cells in tomographic data. INM-ONM intermembrane filaments are indicated with black arrowheads. Right panels show segmentation of lamina filaments (blue lines). Scale bars = 100 nm. **(B)** Immunoblots against nuclear lamina components Lamin A/C (LMNA/C), Lamin B1 (LB1), and Lamin B2/B3 (LB2/B3) using human sperm lysate, with replicates; α-tubulin shown as loading control.

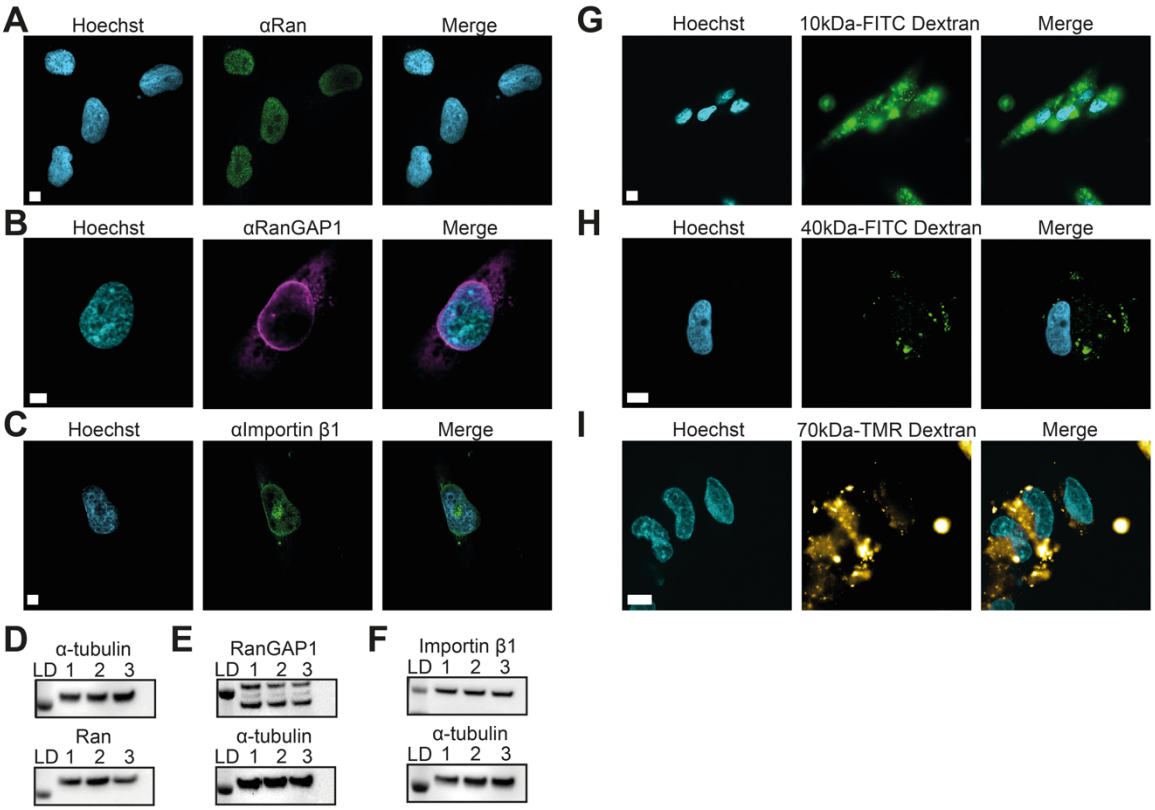

Supplementary Figure 7 – Active transport and diffusion in human fibroblasts. (A-C) Immunofluorescence and confocal imaging different nuclear transport components: Ran showing nuclear localisation during interphase in human fibroblasts **(A)**; RanGAP1 showing localisation to the NE and some cytoplasm signal **(B)**; and Importin β1, showing nuclear signal **(C)**. Scale bars = 5µm. **(D-F)** Western Blots against Ran **(D)**, RanGAP1 **(E)**, and Importin β1 **(F)** using human fibroblasts lysate, shown with replicates and α-tubulin as loading control. **(G-I)** Human fibroblasts treated with digitonin for the delivery of 10kDa-FITC **(G)**, 40kDa-FITC **(H)** and 70kDa-TMR **(I)** dextrans. Signal for 10kDa-FITC Dextran, but not 40kDa-FITC or 70kDa-TMR Dextran, can be observed in the nucleus. Scale bars =5µm.

Supp Movie 1. Overview of the human sperm *in situ* NPC structure. Cryo-EM map (grey) with fitted IR model (PDB:7r5k) shown as cartoon representation (blue), as in Figure 2A.

Supp Movie 2. Intermembrane space filaments adjacent to NPCs in sperm cell NE. Cryo tomogram of a sperm cell NE (segmented in blue) shows filamentous structures (segmented as green cylinders) in the intermembrane space between NPCs. See also Figure 5A and B, and Supp Fig. 5E. Scale bar: 100nm.

REFERENCES

1. Lin, D.H., and Hoelz, A. (2019). The Structure of the Nuclear Pore Complex (An Update). Annu Rev Biochem *88*, 725-783. 10.1146/annurev-biochem-062917-011901.
2. Strambio-De-Castillia, C., Niepel, M., and Rout, M.P. (2010). The nuclear pore complex: bridging nuclear transport and gene regulation. Nat Rev Mol Cell Biol *11*, 490-501. 10.1038/nrm2928.
3. Raices, M., and D'Angelo, M.A. (2017). Nuclear pore complexes and regulation of gene expression. Curr Opin Cell Biol *46*, 26-32. 10.1016/j.ceb.2016.12.006.
4. Hampoelz, B., Andres-Pons, A., Kastritis, P., and Beck, M. (2019). Structure and Assembly of the Nuclear Pore Complex. Annu Rev Biophys *48*, 515-536. 10.1146/annurev-biophys-052118-115308.
5. Huang, G., Zeng, C., and Shi, Y. (2023). Structure of the nuclear pore complex goes atomic. Curr Opin Struct Biol *78*, 102523. 10.1016/j.sbi.2022.102523.
6. Tai, L., Yin, G., Sun, F., and Zhu, Y. (2023). Cryo-electron Microscopy Reveals the Structure of the Nuclear Pore Complex. J Mol Biol *435*, 168051. 10.1016/j.jmb.2023.168051.
7. Zhang, Y., Li, S., Zeng, C., Huang, G., Zhu, X., Wang, Q., Wang, K., Zhou, Q., Yan, C., Zhang, W., et al. (2020). Molecular architecture of the luminal ring of the Xenopus laevis nuclear pore complex. Cell Res *30*, 532-540. 10.1038/s41422-020-0320-y.
8. Bui, K.H., von Appen, A., DiGuilio, A.L., Ori, A., Sparks, L., Mackmull, M.T., Bock, T., Hagen, W., Andres-Pons, A., Glavy, J.S., and Beck, M. (2013). Integrated structural analysis of the human nuclear pore complex scaffold. Cell *155*, 1233-1243. 10.1016/j.cell.2013.10.055.
9. Bley, C.J., Nie, S., Mobbs, G.W., Petrovic, S., Gres, A.T., Liu, X., Mukherjee, S., Harvey, S., Huber, F.M., Lin, D.H., et al. (2022). Architecture of the cytoplasmic face of the nuclear pore. Science *376*, eabm9129. 10.1126/science.abm9129.
10. Fontana, P., Dong, Y., Pi, X., Tong, A.B., Hecksel, C.W., Wang, L., Fu, T.M., Bustamante, C., and Wu, H. (2022). Structure of cytoplasmic ring of nuclear pore complex by integrative cryo-EM and AlphaFold. Science *376*, eabm9326. 10.1126/science.abm9326.
11. Huang, G., Zhang, Y., Zhu, X., Zeng, C., Wang, Q., Zhou, Q., Tao, Q., Liu, M., Lei, J., Yan, C., and Shi, Y. (2020). Structure of the cytoplasmic ring of the Xenopus laevis nuclear pore complex by cryo-electron microscopy single particle analysis. Cell Res *30*, 520-531. 10.1038/s41422-020-0319-4.
12. Zhu, X., Huang, G., Zeng, C., Zhan, X., Liang, K., Xu, Q., Zhao, Y., Wang, P., Wang, Q., Zhou, Q., et al. (2022). Structure of the cytoplasmic ring of the Xenopus laevis nuclear pore complex. Science *376*, eabl8280. 10.1126/science.abl8280.
13. Mosalaganti, S., Obarska-Kosinska, A., Siggel, M., Taniguchi, R., Turonova, B., Zimmerli, C.E., Buczak, K., Schmidt, F.H., Margiotta, E., Mackmull, M.T., et al. (2022). AI-based structure prediction empowers integrative structural analysis of human nuclear pores. Science *376*, eabm9506. 10.1126/science.abm9506.
14. Otsuka, S., Bui, K.H., Schorb, M., Hossain, M.J., Politi, A.Z., Koch, B., Eltsov, M., Beck, M., and Ellenberg, J. (2016). Nuclear pore assembly proceeds by an inside-out extrusion of the nuclear envelope. Elife *5*. 10.7554/eLife.19071.

15. Otsuka, S., Tempkin, J.O.B., Zhang, W., Politi, A.Z., Rybina, A., Hossain, M.J., Kueblbeck, M., Callegari, A., Koch, B., Morero, N.R., et al. (2023). A quantitative map of nuclear pore assembly reveals two distinct mechanisms. Nature *613*, 575-581. 10.1038/s41586-022-05528-w.
16. Singh, D., Soni, N., Hutchings, J., Echeverria, I., Shaikh, F., Duquette, M., Suslov, S., Li, Z., van Eeuwen, T., Molloy, K., et al. (2024). The molecular architecture of the nuclear basket. Cell. 10.1016/j.cell.2024.07.020.
17. Lee, E.S., Wolf, E.J., Ihn, S.S.J., Smith, H.W., Emili, A., and Palazzo, A.F. (2020). TPR is required for the efficient nuclear export of mRNAs and lncRNAs from short and intron-poor genes. Nucleic Acids Res *48*, 11645-11663. 10.1093/nar/gkaa919.
18. Li, Y., Aksenova, V., Tingey, M., Yu, J., Ma, P., Arnaoutov, A., Chen, S., Dasso, M., and Yang, W. (2021). Distinct roles of nuclear basket proteins in directing the passage of mRNA through the nuclear pore. Proc Natl Acad Sci U S A *118*. 10.1073/pnas.2015621118.
19. Walther, T.C., Fornerod, M., Pickersgill, H., Goldberg, M., Allen, T.D., and Mattaj, I.W. (2001). The nucleoporin Nup153 is required for nuclear pore basket formation, nuclear pore complex anchoring and import of a subset of nuclear proteins. EMBO J *20*, 5703-5714. 10.1093/emboj/20.20.5703.
20. Knockenhauer, K.E., and Schwartz, T.U. (2016). The Nuclear Pore Complex as a Flexible and Dynamic Gate. Cell *164*, 1162-1171. 10.1016/j.cell.2016.01.034.
21. Kabachinski, G., and Schwartz, T.U. (2015). The nuclear pore complex--structure and function at a glance. J Cell Sci *128*, 423-429. 10.1242/jcs.083246.
22. Wente, S.R., and Rout, M.P. (2010). The nuclear pore complex and nuclear transport. Cold Spring Harb Perspect Biol *2*, a000562. 10.1101/cshperspect.a000562.
23. Terry, L.J., Shows, E.B., and Wente, S.R. (2007). Crossing the nuclear envelope: hierarchical regulation of nucleocytoplasmic transport. Science *318*, 1412-1416. 10.1126/science.1142204.
24. Gorlich, D., and Kutay, U. (1999). Transport between the cell nucleus and the cytoplasm. Annu Rev Cell Dev Biol *15*, 607-660. 10.1146/annurev.cellbio.15.1.607.
25. Mattaj, I.W., and Englmeier, L. (1998). Nucleocytoplasmic transport: the soluble phase. Annu Rev Biochem *67*, 265-306. 10.1146/annurev.biochem.67.1.265.
26. von Appen, A., Kosinski, J., Sparks, L., Ori, A., DiGuilio, A.L., Vollmer, B., Mackmull, M.T., Banterle, N., Parca, L., Kastritis, P., et al. (2015). In situ structural analysis of the human nuclear pore complex. Nature *526*, 140-143. 10.1038/nature15381.
27. Hutten, S., Flotho, A., Melchior, F., and Kehlenbach, R.H. (2008). The Nup358-RanGAP complex is required for efficient importin alpha/beta-dependent nuclear import. Mol Biol Cell *19*, 2300-2310. 10.1091/mbc.e07-12-1279.
28. Hampoelz, B., Mackmull, M.T., Machado, P., Ronchi, P., Bui, K.H., Schieber, N., Santarella-Mellwig, R., Necakov, A., Andres-Pons, A., Philippe, J.M., et al. (2016). Pre-assembled Nuclear Pores Insert into the Nuclear Envelope during Early Development. Cell *166*, 664-678. 10.1016/j.cell.2016.06.015.

29. Kessel, R.G. (1983). The structure and function of annulate lamellae: porous cytoplasmic and intranuclear membranes. Int Rev Cytol *82*, 181-303. 10.1016/s0074-7696(08)60826-8.
30. Hampoelz, B., Schwarz, A., Ronchi, P., Bragulat-Teixidor, H., Tischer, C., Gaspar, I., Ephrussi, A., Schwab, Y., and Beck, M. (2019). Nuclear Pores Assemble from Nucleoporin Condensates During Oogenesis. Cell *179*, 671-686 e617. 10.1016/j.cell.2019.09.022.
31. Sachweh, J., Börmel, M., Klumpe, S., Becker, A., Taniguchi, R., Kubańska, M.A., Pintschovius, V., Kaindl, E., Plitzko, J.M., Wilfling, F., et al. (2024). The small GTPase Ran defines Nuclear Pore Complex Asymmetry. bioRxiv, 2024.2010.2010.617378. 10.1101/2024.10.10.617378.
32. Ren, H., Xin, G., Jia, M., Zhu, S., Lin, Q., Wang, X., Jiang, Q., and Zhang, C. (2019). Postmitotic annulate lamellae assembly contributes to nuclear envelope reconstitution in daughter cells. J Biol Chem *294*, 10383-10391. 10.1074/jbc.AC119.008171.
33. Chemes, H.E., Fawcett, D.W., and Dym, M. (1978). Unusual features of the nuclear envelope in human spermatogenic cells. Anat Rec *192*, 493-512. 10.1002/ar.1091920404.
34. Sun, C.N., Chew, E.C., and White, H.J. (1977). Cytoplasmic annulate lamellae and intranuclear membranes in human spermatids and sperm. Cell Biol Int Rep *1*, 345-351. 10.1016/0309-1651(77)90064-9.
35. Mahamid, J., Pfeffer, S., Schaffer, M., Villa, E., Danev, R., Cuellar, L.K., Forster, F., Hyman, A.A., Plitzko, J.M., and Baumeister, W. (2016). Visualizing the molecular sociology at the HeLa cell nuclear periphery. Science *351*, 969-972. 10.1126/science.aad8857.
36. Mosalaganti, S., Kosinski, J., Albert, S., Schaffer, M., Strenkert, D., Salome, P.A., Merchant, S.S., Plitzko, J.M., Baumeister, W., Engel, B.D., and Beck, M. (2018). In situ architecture of the algal nuclear pore complex. Nat Commun *9*, 2361. 10.1038/s41467-018-04739-y.
37. Akey, C.W., Singh, D., Ouch, C., Echeverria, I., Nudelman, I., Varberg, J.M., Yu, Z., Fang, F., Shi, Y., Wang, J., et al. (2022). Comprehensive structure and functional adaptations of the yeast nuclear pore complex. Cell *185*, 361-378 e325. 10.1016/j.cell.2021.12.015.
38. Allegretti, M., Zimmerli, C.E., Rantos, V., Wilfling, F., Ronchi, P., Fung, H.K.H., Lee, C.W., Hagen, W., Turonova, B., Karius, K., et al. (2020). In-cell architecture of the nuclear pore and snapshots of its turnover. Nature *586*, 796-800. 10.1038/s41586-020-2670-5.
39. Schuller, A.P., Wojtynek, M., Mankus, D., Tatli, M., Kronenberg-Tenga, R., Regmi, S.G., Dip, P.V., Lytton-Jean, A.K.R., Brignole, E.J., Dasso, M., et al. (2021). The cellular environment shapes the nuclear pore complex architecture. Nature *598*, 667-671. 10.1038/s41586-021-03985-3.
40. Zimmerli, C.E., Allegretti, M., Rantos, V., Goetz, S.K., Obarska-Kosinska, A., Zagoriy, I., Halavatyi, A., Hummer, G., Mahamid, J., Kosinski, J., and Beck, M. (2021). Nuclear pores dilate and constrict in cellulo. Science *374*, eabd9776. 10.1126/science.abd9776.
41. Elosegui-Artola, A., Andreu, I., Beedle, A.E.M., Lezamiz, A., Uroz, M., Kosmalska, A.J., Oria, R., Kechagia, J.Z., Rico-Lastres, P., Le Roux, A.L., et al. (2017). Force

Triggers YAP Nuclear Entry by Regulating Transport across Nuclear Pores. Cell *171*, 1397-1410 e1314. 10.1016/j.cell.2017.10.008.
42. Kreysing, J.P., Heidari, M., Zila, V., Cruz-Leon, S., Obarska-Kosinska, A., Laketa, V., Welsch, S., Köfinger, J., Turoňová, B., Hummer, G., et al. (2024). Passage of the HIV capsid cracks the nuclear pore. bioRxiv, 2024.2004.2023.590733. 10.1101/2024.04.23.590733.
43. Shen, W., Gong, B., Xing, C., Zhang, L., Sun, J., Chen, Y., Yang, C., Yan, L., Chen, L., Yao, L., et al. (2022). Comprehensive maturity of nuclear pore complexes regulates zygotic genome activation. Cell *185*, 4954-4970.e4920. https://doi.org/10.1016/j.cell.2022.11.011.
44. Taniguchi, R., Orniacki, C., Kreysing, J.P., Zila, V., Zimmerli, C.E., Böhm, S., Turoňová, B., Kräusslich, H.-G., Doye, V., and Beck, M. (2024). Nuclear pores safeguard the integrity of the nuclear envelope. bioRxiv, 2024.2002.2005.578890. 10.1101/2024.02.05.578890.
45. Kim, S.J., Fernandez-Martinez, J., Nudelman, I., Shi, Y., Zhang, W., Raveh, B., Herricks, T., Slaughter, B.D., Hogan, J.A., Upla, P., et al. (2018). Integrative structure and functional anatomy of a nuclear pore complex. Nature *555*, 475-482. 10.1038/nature26003.
46. Morgan, K.J., Carley, E., Coyne, A.N., Rothstein, J.D., Lusk, C.P., and King, M.C. (2024). Visualizing nuclear pore complex plasticity with Pan-Expansion Microscopy. bioRxiv, 2024.2009.2018.613744. 10.1101/2024.09.18.613744.
47. Pajerowski, J.D., Dahl, K.N., Zhong, F.L., Sammak, P.J., and Discher, D.E. (2007). Physical plasticity of the nucleus in stem cell differentiation. Proc Natl Acad Sci U S A *104*, 15619-15624. 10.1073/pnas.0702576104.
48. Friedl, P., Wolf, K., and Lammerding, J. (2011). Nuclear mechanics during cell migration. Curr Opin Cell Biol *23*, 55-64. 10.1016/j.ceb.2010.10.015.
49. Lehti, M.S., and Sironen, A. (2016). Formation and function of the manchette and flagellum during spermatogenesis. Reproduction *151*, R43-54. 10.1530/REP-15-0310.
50. O'Donnell, L. (2014). Mechanisms of spermiogenesis and spermiation and how they are disturbed. Spermatogenesis *4*, e979623. 10.4161/21565562.2014.979623.
51. Pereira, C.D., Serrano, J.B., Martins, F., da Cruz, E.S.O.A.B., and Rebelo, S. (2019). Nuclear envelope dynamics during mammalian spermatogenesis: new insights on male fertility. Biol Rev Camb Philos Soc *94*, 1195-1219. 10.1111/brv.12498.
52. Morgan, M., Kumar, L., Li, Y., and Baptissart, M. (2021). Post-transcriptional regulation in spermatogenesis: all RNA pathways lead to healthy sperm. Cell Mol Life Sci *78*, 8049-8071. 10.1007/s00018-021-04012-4.
53. Major, A.T., Whiley, P.A., and Loveland, K.L. (2011). Expression of nucleocytoplasmic transport machinery: clues to regulation of spermatogenic development. Biochim Biophys Acta *1813*, 1668-1688. 10.1016/j.bbamcr.2011.03.008.
54. Whiley, P.A., Miyamoto, Y., McLachlan, R.I., Jans, D.A., and Loveland, K.L. (2012). Changing subcellular localization of nuclear transport factors during human spermatogenesis. Int J Androl *35*, 158-169. 10.1111/j.1365-2605.2011.01202.x.

55. Fawcett, D.W., and Chemes, H.E. (1979). Changes in distribution of nuclear pores during differentiation of the male germ cells. Tissue Cell *11*, 147-162. 10.1016/0040-8166(79)90015-6.
56. Ho, H.C. (2010). Redistribution of nuclear pores during formation of the redundant nuclear envelope in mouse spermatids. J Anat *216*, 525-532. 10.1111/j.1469-7580.2009.01204.x.
57. Arafah, K., Lopez, F., Cazin, C., Kherraf, Z.E., Tassistro, V., Loundou, A., Arnoult, C., Thierry-Mieg, N., Bulet, P., Guichaoua, M.R., and Ray, P.F. (2021). Defect in the nuclear pore membrane glycoprotein 210-like gene is associated with extreme uncondensed sperm nuclear chromatin and male infertility: a case report. Hum Reprod *36*, 693-701. 10.1093/humrep/deaa329.
58. Guglielmi, V., Sakuma, S., and D'Angelo, M.A. (2020). Nuclear pore complexes in development and tissue homeostasis. Development *147*. 10.1242/dev.183442.
59. Lai, T.H., Wu, Y.Y., Wang, Y.Y., Chen, M.F., Wang, P., Chen, T.M., Wu, Y.N., Chiang, H.S., Kuo, P.L., and Lin, Y.H. (2016). SEPT12-NDC1 Complexes Are Required for Mammalian Spermiogenesis. Int J Mol Sci *17*. 10.3390/ijms17111911.
60. Miyamoto, Y., Boag, P.R., Hime, G.R., and Loveland, K.L. (2012). Regulated nucleocytoplasmic transport during gametogenesis. Biochim Biophys Acta *1819*, 616-630. 10.1016/j.bbagrm.2012.01.015.
61. Scheffler, K., Uraji, J., Jentoft, I., Cavazza, T., Mönnich, E., Mogessie, B., and Schuh, M. (2021). Two mechanisms drive pronuclear migration in mouse zygotes. Nature Communications *12*, 841. 10.1038/s41467-021-21020-x.
62. Cavazza, T., Takeda, Y., Politi, A.Z., Aushev, M., Aldag, P., Baker, C., Choudhary, M., Bucevičius, J., Lukinavičius, G., Elder, K., et al. (2021). Parental genome unification is highly error-prone in mammalian embryos. Cell *184*, 2860-2877.e2822. 10.1016/j.cell.2021.04.013.
63. Crimmins, S., Sutovsky, M., Chen, P.C., Huffman, A., Wheeler, C., Swing, D.A., Roth, K., Wilson, J., Sutovsky, P., and Wilson, S. (2009). Transgenic rescue of ataxia mice reveals a male-specific sterility defect. Dev Biol *325*, 33-42. 10.1016/j.ydbio.2008.09.021.
64. Maul, G.G., and Deaven, L. (1977). Quantitative determination of nuclear pore complexes in cycling cells with differing DNA content. J Cell Biol *73*, 748-760. 10.1083/jcb.73.3.748.
65. Dultz, E., and Ellenberg, J. (2010). Live imaging of single nuclear pores reveals unique assembly kinetics and mechanism in interphase. J Cell Biol *191*, 15-22. 10.1083/jcb.201007076.
66. Maeshima, K., Iino, H., Hihara, S., Funakoshi, T., Watanabe, A., Nishimura, M., Nakatomi, R., Yahata, K., Imamoto, F., Hashikawa, T., et al. (2010). Nuclear pore formation but not nuclear growth is governed by cyclin-dependent kinases (Cdks) during interphase. Nat Struct Mol Biol *17*, 1065-1071. 10.1038/nsmb.1878.
67. Zila, V., Margiotta, E., Turonova, B., Muller, T.G., Zimmerli, C.E., Mattei, S., Allegretti, M., Borner, K., Rada, J., Muller, B., et al. (2021). Cone-shaped HIV-1 capsids are transported through intact nuclear pores. Cell *184*, 1032-1046 e1018. 10.1016/j.cell.2021.01.025.

68. Walther, T.C., Alves, A., Pickersgill, H., Loiodice, I., Hetzer, M., Galy, V., Hulsmann, B.B., Kocher, T., Wilm, M., Allen, T., et al. (2003). The conserved Nup107-160 complex is critical for nuclear pore complex assembly. Cell *113*, 195-206. 10.1016/s0092-8674(03)00235-6.
69. Kucinska, M.K., Fedry, J., Galli, C., Morone, D., Raimondi, A., Solda, T., Forster, F., and Molinari, M. (2023). TMX4-driven LINC complex disassembly and asymmetric autophagy of the nuclear envelope upon acute ER stress. Nat Commun *14*, 3497. 10.1038/s41467-023-39172-3.
70. Barad, B.A., Medina, M., Fuentes, D., Wiseman, R.L., and Grotjahn, D.A. (2023). Quantifying organellar ultrastructure in cryo-electron tomography using a surface morphometrics pipeline. J Cell Biol *222*. 10.1083/jcb.202204093.
71. Turgay, Y., Eibauer, M., Goldman, A.E., Shimi, T., Khayat, M., Ben-Harush, K., Dubrovsky-Gaupp, A., Sapra, K.T., Goldman, R.D., and Medalia, O. (2017). The molecular architecture of lamins in somatic cells. Nature *543*, 261-264. 10.1038/nature21382.
72. Eibauer, M., Weber, M.S., Kronenberg-Tenga, R., Beales, C.T., Boujemaa-Paterski, R., Turgay, Y., Sivagurunathan, S., Kraxner, J., Koster, S., Goldman, R.D., and Medalia, O. (2024). Vimentin filaments integrate low-complexity domains in a complex helical structure. Nat Struct Mol Biol *31*, 939-949. 10.1038/s41594-024-01261-2.
73. Lin, Y.-H., Kuo, Y.-C., Chiang, H.-S., and Kuo, P.-L. (2011). The role of the septin family in spermiogenesis. Spermatogenesis *1*, 298-302. 10.4161/spmg.1.4.18326.
74. Lin, Y.H., Lin, Y.M., Wang, Y.Y., Yu, I.S., Lin, Y.W., Wang, Y.H., Wu, C.M., Pan, H.A., Chao, S.C., Yen, P.H., et al. (2009). The expression level of septin12 is critical for spermiogenesis. Am J Pathol *174*, 1857-1868. 10.2353/ajpath.2009.080955.
75. Kuo, Y.C., Lin, Y.H., Chen, H.I., Wang, Y.Y., Chiou, Y.W., Lin, H.H., Pan, H.A., Wu, C.M., Su, S.M., Hsu, C.C., and Kuo, P.L. (2012). SEPT12 mutations cause male infertility with defective sperm annulus. Hum Mutat *33*, 710-719. 10.1002/humu.22028.
76. Chen, H., Li, P., Du, X., Zhao, Y., Wang, L., Tian, Y., Song, X., Shuai, L., Bai, X., and Chen, L. (2022). Homozygous Loss of Septin12, but not its Haploinsufficiency, Leads to Male Infertility and Fertilization Failure. Front Cell Dev Biol *10*, 850052. 10.3389/fcell.2022.850052.
77. Lin, Y.H., Chou, C.K., Hung, Y.C., Yu, I.S., Pan, H.A., Lin, S.W., and Kuo, P.L. (2011). SEPT12 deficiency causes sperm nucleus damage and developmental arrest of preimplantation embryos. Fertil Steril *95*, 363-365. 10.1016/j.fertnstert.2010.07.1064.
78. Shen, Y.R., Wang, H.Y., Kuo, Y.C., Shih, S.C., Hsu, C.H., Chen, Y.R., Wu, S.R., Wang, C.Y., and Kuo, P.L. (2017). SEPT12 phosphorylation results in loss of the septin ring/sperm annulus, defective sperm motility and poor male fertility. PLoS Genet *13*, e1006631. 10.1371/journal.pgen.1006631.
79. Lin, Y.H., Wang, Y.Y., Chen, H.I., Kuo, Y.C., Chiou, Y.W., Lin, H.H., Wu, C.M., Hsu, C.C., Chiang, H.S., and Kuo, P.L. (2012). SEPTIN12 genetic variants confer susceptibility to teratozoospermia. PLoS One *7*, e34011. 10.1371/journal.pone.0034011.

80. Yeh, C.H., Kuo, P.L., Wang, Y.Y., Wu, Y.Y., Chen, M.F., Lin, D.Y., Lai, T.H., Chiang, H.S., and Lin, Y.H. (2015). SEPT12/SPAG4/LAMINB1 complexes are required for maintaining the integrity of the nuclear envelope in postmeiotic male germ cells. PLoS One *10*, e0120722. 10.1371/journal.pone.0120722.
81. Sanovec, O., Frolikova, M., Kraus, V., Vondrakova, J., Qasemi, M., Spevakova, D., Simonik, O., Moritz, L., Caswell, D.L., Liska, F., et al. (2024). Protamine 2 Deficiency Results In Septin 12 Abnormalities. bioRxiv. 10.1101/2024.05.28.596175.
82. Sirajuddin, M., Farkasovsky, M., Hauer, F., Kuhlmann, D., Macara, I.G., Weyand, M., Stark, H., and Wittinghofer, A. (2007). Structural insight into filament formation by mammalian septins. Nature *449*, 311-315. 10.1038/nature06052.
83. Mostowy, S., and Cossart, P. (2012). Septins: the fourth component of the cytoskeleton. Nature Reviews Molecular Cell Biology *13*, 183-194. 10.1038/nrm3284.
84. Tanaka-Takiguchi, Y., Kinoshita, M., and Takiguchi, K. (2009). Septin-mediated uniform bracing of phospholipid membranes. Curr Biol *19*, 140-145. 10.1016/j.cub.2008.12.030.
85. Campello, R.J.G.B., Moulavi, D., and Sander, J. (2013). Density-Based Clustering Based on Hierarchical Density Estimates. held in Berlin, Heidelberg, 2013//. J. Pei, V.S. Tseng, L. Cao, H. Motoda, and G. Xu, eds. (Springer Berlin Heidelberg), pp. 160-172.
86. Cavini, I.A., Leonardo, D.A., Rosa, H.V.D., Castro, D., D'Muniz Pereira, H., Valadares, N.F., Araujo, A.P.U., and Garratt, R.C. (2021). The Structural Biology of Septins and Their Filaments: An Update. Front Cell Dev Biol *9*, 765085. 10.3389/fcell.2021.765085.
87. Kuo, Y.C., Shen, Y.R., Chen, H.I., Lin, Y.H., Wang, Y.Y., Chen, Y.R., Wang, C.Y., and Kuo, P.L. (2015). SEPT12 orchestrates the formation of mammalian sperm annulus by organizing core octameric complexes with other SEPT proteins. J Cell Sci *128*, 923-934. 10.1242/jcs.158998.
88. Mahajan, R., Gerace, L., and Melchior, F. (1998). Molecular characterization of the SUMO-1 modification of RanGAP1 and its role in nuclear envelope association. J Cell Biol *140*, 259-270. 10.1083/jcb.140.2.259.
89. Matunis, M.J., Wu, J., and Blobel, G. (1998). SUMO-1 modification and its role in targeting the Ran GTPase-activating protein, RanGAP1, to the nuclear pore complex. J Cell Biol *140*, 499-509. 10.1083/jcb.140.3.499.
90. Kelley, K., Knockenhauer, K.E., Kabachinski, G., and Schwartz, T.U. (2015). Atomic structure of the Y complex of the nuclear pore. Nat Struct Mol Biol *22*, 425-431. 10.1038/nsmb.2998.
91. Castillo, J., Bogle, O.A., Jodar, M., Torabi, F., Delgado-Duenas, D., Estanyol, J.M., Ballesca, J.L., Miller, D., and Oliva, R. (2019). Proteomic Changes in Human Sperm During Sequential in vitro Capacitation and Acrosome Reaction. Front Cell Dev Biol *7*, 295. 10.3389/fcell.2019.00295.
92. Li, S., Ao, L., Yan, Y., Jiang, J., Chen, B., Duan, Y., Shen, F., Chen, J., Inglis, B., Ni, R., et al. (2019). Differential motility parameters and identification of proteomic profiles of human sperm cryopreserved with cryostraw and cryovial. Clin Proteomics *16*, 24. 10.1186/s12014-019-9244-2.

93. Yang, W.X., Jefferson, H., and Sperry, A.O. (2006). The molecular motor KIFC1 associates with a complex containing nucleoporin NUP62 that is regulated during development and by the small GTPase RAN. Biol Reprod *74*, 684-690. 10.1095/biolreprod.105.049312.
94. Kutay, U., Juhlen, R., and Antonin, W. (2021). Mitotic disassembly and reassembly of nuclear pore complexes. Trends Cell Biol *31*, 1019-1033. 10.1016/j.tcb.2021.06.011.
95. Kinoshita, N., Kimura, K., Matsumoto, N., Watanabe, M., Fukaya, M., and Ide, C. (2004). Mammalian septin Sept2 modulates the activity of GLAST, a glutamate transporter in astrocytes. Genes Cells *9*, 1-14. 10.1111/j.1356-9597.2004.00696.x.
96. Mostowy, S., Janel, S., Forestier, C., Roduit, C., Kasas, S., Pizarro-Cerda, J., Cossart, P., and Lafont, F. (2011). A role for septins in the interaction between the Listeria monocytogenes INVASION PROTEIN InlB and the Met receptor. Biophys J *100*, 1949-1959. 10.1016/j.bpj.2011.02.040.
97. Barral, Y., Mermall, V., Mooseker, M.S., and Snyder, M. (2000). Compartmentalization of the cell cortex by septins is required for maintenance of cell polarity in yeast. Mol Cell *5*, 841-851. 10.1016/s1097-2765(00)80324-x.
98. Szuba, A., Bano, F., Castro-Linares, G., Iv, F., Mavrakis, M., Richter, R.P., Bertin, A., and Koenderink, G.H. (2021). Membrane binding controls ordered self-assembly of animal septins. Elife *10*. 10.7554/eLife.63349.
99. Yeh, C.H., Wang, Y.Y., Wee, S.K., Chen, M.F., Chiang, H.S., Kuo, P.L., and Lin, Y.H. (2019). Testis-Specific SEPT12 Expression Affects SUN Protein Localization and is Involved in Mammalian Spermiogenesis. Int J Mol Sci *20*. 10.3390/ijms20051163.
100. Andreu, I., Granero-Moya, I., Chahare, N.R., Clein, K., Molina-Jordan, M., Beedle, A.E.M., Elosegui-Artola, A., Abenza, J.F., Rossetti, L., Trepat, X., et al. (2022). Mechanical force application to the nucleus regulates nucleocytoplasmic transport. Nat Cell Biol *24*, 896-905. 10.1038/s41556-022-00927-7.
101. Forler, D., Rabut, G., Ciccarelli, F.D., Herold, A., Kocher, T., Niggeweg, R., Bork, P., Ellenberg, J., and Izaurralde, E. (2004). RanBP2/Nup358 provides a major binding site for NXF1-p15 dimers at the nuclear pore complex and functions in nuclear mRNA export. Mol Cell Biol *24*, 1155-1167. 10.1128/MCB.24.3.1155-1167.2004.
102. Ori, A., Banterle, N., Iskar, M., Andres-Pons, A., Escher, C., Khanh Bui, H., Sparks, L., Solis-Mezarino, V., Rinner, O., Bork, P., et al. (2013). Cell type-specific nuclear pores: a case in point for context-dependent stoichiometry of molecular machines. Mol Syst Biol *9*, 648. 10.1038/msb.2013.4.
103. Sabri, N., Roth, P., Xylourgidis, N., Sadeghifar, F., Adler, J., and Samakovlis, C. (2007). Distinct functions of the Drosophila Nup153 and Nup214 FG domains in nuclear protein transport. J Cell Biol *178*, 557-565. 10.1083/jcb.200612135.
104. Xylourgidis, N., Roth, P., Sabri, N., Tsarouhas, V., and Samakovlis, C. (2006). The nucleoporin Nup214 sequesters CRM1 at the nuclear rim and modulates NFkappaB activation in Drosophila. J Cell Sci *119*, 4409-4419. 10.1242/jcs.03201.

105. Bischoff, F.R., Klebe, C., Kretschmer, J., Wittinghofer, A., and Ponstingl, H. (1994). RanGAP1 induces GTPase activity of nuclear Ras-related Ran. Proc Natl Acad Sci U S A *91*, 2587-2591. 10.1073/pnas.91.7.2587.
106. Weis, K. (1998). Importins and exportins: how to get in and out of the nucleus. Trends Biochem Sci *23*, 185-189. 10.1016/s0968-0004(98)01204-3.
107. Kierszenbaum, A.L., Gil, M., Rivkin, E., and Tres, L.L. (2002). Ran, a GTP-binding protein involved in nucleocytoplasmic transport and microtubule nucleation, relocates from the manchette to the centrosome region during rat spermiogenesis. Mol Reprod Dev *63*, 131-140. 10.1002/mrd.10164.
108. Ben-Efraim, I., Frosst, P.D., and Gerace, L. (2009). Karyopherin binding interactions and nuclear import mechanism of nuclear pore complex protein Tpr. BMC Cell Biol *10*, 74. 10.1186/1471-2121-10-74.
109. Bayliss, R., Littlewood, T., and Stewart, M. (2000). Structural basis for the interaction between FxFG nucleoporin repeats and importin-beta in nuclear trafficking. Cell *102*, 99-108. 10.1016/s0092-8674(00)00014-3.
110. Raices, M., and D'Angelo, M.A. (2012). Nuclear pore complex composition: a new regulator of tissue-specific and developmental functions. Nat Rev Mol Cell Biol *13*, 687-699. 10.1038/nrm3461.
111. Wagner, F.R., Watanabe, R., Schampers, R., Singh, D., Persoon, H., Schaffer, M., Fruhstorfer, P., Plitzko, J., and Villa, E. (2020). Preparing samples from whole cells using focused-ion-beam milling for cryo-electron tomography. Nat Protoc *15*, 2041-2070. 10.1038/s41596-020-0320-x.
112. Sexton, D.L., Burgold, S., Schertel, A., and Tocheva, E.I. (2022). Super-resolution confocal cryo-CLEM with cryo-FIB milling for in situ imaging of Deinococcus radiodurans. Curr Res Struct Biol *4*, 1-9. 10.1016/j.crstbi.2021.12.001.
113. Eisenstein, F., Yanagisawa, H., Kashihara, H., Kikkawa, M., Tsukita, S., and Danev, R. (2023). Parallel cryo electron tomography on in situ lamellae. Nat Methods *20*, 131-138. 10.1038/s41592-022-01690-1.
114. Hagen, W.J.H., Wan, W., and Briggs, J.A.G. (2017). Implementation of a cryo-electron tomography tilt-scheme optimized for high resolution subtomogram averaging. J Struct Biol *197*, 191-198. 10.1016/j.jsb.2016.06.007.
115. Tegunov, D., and Cramer, P. (2019). Real-time cryo-electron microscopy data preprocessing with Warp. Nat Methods *16*, 1146-1152. 10.1038/s41592-019-0580-y.
116. Zheng, S., Wolff, G., Greenan, G., Chen, Z., Faas, F.G.A., Barcena, M., Koster, A.J., Cheng, Y., and Agard, D.A. (2022). AreTomo: An integrated software package for automated marker-free, motion-corrected cryo-electron tomographic alignment and reconstruction. J Struct Biol X *6*, 100068. 10.1016/j.yjsbx.2022.100068.
117. Kremer, J.R., Mastronarde, D.N., and McIntosh, J.R. (1996). Computer visualization of three-dimensional image data using IMOD. J Struct Biol *116*, 71-76. 10.1006/jsbi.1996.0013.
118. Burt, A. (2024). Script for converting dipole annotations as IMOD model files into oriented particles compatible with Warp. Zenodo. 10.5281/zenodo.14010295.
119. Zivanov, J., Nakane, T., Forsberg, B.O., Kimanius, D., Hagen, W.J., Lindahl, E., and Scheres, S.H. (2018). New tools for automated high-resolution cryo-EM structure determination in RELION-3. Elife *7*. 10.7554/eLife.42166.

120. Dendooven, T., Yatskevich, S., Burt, A., Chen, Z.A., Bellini, D., Rappsilber, J., Kilmartin, J.V., and Barford, D. (2024). Structure of the native gamma-tubulin ring complex capping spindle microtubules. Nat Struct Mol Biol *31*, 1134-1144. 10.1038/s41594-024-01281-y.
121. Castano-Diez, D., Kudryashev, M., Arheit, M., and Stahlberg, H. (2012). Dynamo: a flexible, user-friendly development tool for subtomogram averaging of cryo-EM data in high-performance computing environments. J Struct Biol *178*, 139-151. 10.1016/j.jsb.2011.12.017.
122. Burt, A., Gaifas, L., Dendooven, T., and Gutsche, I. (2021). A flexible framework for multi-particle refinement in cryo-electron tomography. PLoS Biol *19*, e3001319. 10.1371/journal.pbio.3001319.
123. Tegunov, D., Xue, L., Dienemann, C., Cramer, P., and Mahamid, J. (2021). Multi-particle cryo-EM refinement with M visualizes ribosome-antibiotic complex at 3.5 A in cells. Nat Methods *18*, 186-193. 10.1038/s41592-020-01054-7.